nature cell biology

Activator–inhibitor coupling between Rho signalling and actin assembly makes the cell cortex an excitable medium

William M. Bement[1,6,7,8], Marcin Leda[2], Alison M. Moe[1], Angela M. Kita[1], Matthew E. Larson[1], Adriana E. Golding[1], Courtney Pfeuti[1], Kuan-Chung Su[3], Ann L. Miller[4], Andrew B. Goryachev[2,7,8] and George von Dassow[5,6,7,8]

Animal cell cytokinesis results from patterned activation of the small GTPase Rho, which directs assembly of actomyosin in the equatorial cortex. Cytokinesis is restricted to a portion of the cell cycle following anaphase onset in which the cortex is responsive to signals from the spindle. We show that shortly after anaphase onset oocytes and embryonic cells of frogs and echinoderms exhibit cortical waves of Rho activity and F-actin polymerization. The waves are modulated by cyclin-dependent kinase 1 (Cdk1) activity and require the Rho GEF (guanine nucleotide exchange factor), Ect2. Surprisingly, during wave propagation, although Rho activity elicits F-actin assembly, F-actin subsequently inactivates Rho. Experimental and modelling results show that waves represent excitable dynamics of a reaction–diffusion system with Rho as the activator and F-actin the inhibitor. We propose that cortical excitability explains fundamental features of cytokinesis including its cell cycle regulation.

Cytokinesis begins with activation of Rho in a narrow zone at the plasma membrane[1]. Rho directs assembly of the cytokinetic apparatus, a transient array of F-actin and myosin-2. Spindle-derived cues specify the Rho zone; accordingly, considerable effort has been directed at characterization of these signals and their transport. The current consensus is that the centralspindlin complex interprets spindle microtubule organization to concentrate Ect2 at the equator, thus defining the Rho zone[2,3].

The cortex is not a passive substrate in cytokinesis, but rather may actively process and amplify spindle-derived signals during a discrete window of the cell cycle. Physical manipulations of echinoderm embryos showed that the cortex becomes responsive (as manifest by furrowing) shortly after anaphase onset and remains so until shortly before the next M-phase[4] whereas experimental M-phase arrest prevents development of this responsiveness[5]. Similarly, manipulations of cultured mammalian cells showed that forced anaphase entry results in ~50 min of ectopic cortical contractility even after ablation of the spindle, leading to the concept of 'C-phase' ('cytokinetic phase'), a period of the cell cycle during which large-scale cortical contractility can be focused by signalling[6].

Here we describe the discovery of a cell-cycle-entrained behaviour that we propose reflects the capacity of the cortex to support cytokinesis—cortical excitability. This behaviour is manifest as mutually coordinated cortical waves of Rho activity and F-actin assembly that are Ect2-dependent and modulated by cyclin-dependent kinase 1 (Cdk1). We show that cortical excitability is present in vertebrates and invertebrates, that it coincides with the ability of different cells to respond to spindle signals, and that it involves F-actin-dependent Rho inactivation.

RESULTS

Cortical F-actin waves in activated *Xenopus* eggs and embryos

Previous low-resolution imaging of cytokinesis in *Xenopus* embryos revealed cortical 'flickers' of F-actin outside the furrow[7]. Remarkably, when imaged at higher resolution, the flickers resolved into waves of F-actin (Fig. 1a,b and Supplementary Videos 1 and 2), similar to those previously described in chemotactic cells[8]. F-actin waves can be detected using two different F-actin probes, UtrCH (ref. 9; Fig. 1a,b) or Lifeact[10] (see Supplementary Fig. 1a). Apparently identical structures exist in fixed, uninjected embryos stained with phalloidin (Fig. 1c),

[1]Laboratory of Cell and Molecular Biology, Graduate Program in Cell and Molecular Biology, University of Wisconsin-Madison, Madison, Wisconsin 53706, USA. [2]Centre for Synthetic and Systems Biology, University of Edinburgh, Edinburgh EH9 3BF, UK. [3]Whitehead Institute for Biomedical Research, Massachusetts Institute of Technology, Boston, Massachusetts 02142, USA. [4]Department of Molecular, Cellular and Developmental Biology, University of Michigan, Ann Arbor, Michigan 48190, USA. [5]Oregon Institute of Marine Biology, University of Oregon, Charleston, Oregon 97420, USA. [6]These authors contributed equally to this work. [7]These authors jointly supervised this work.
[8]Correspondence should be addressed to W.M.B., A.B.G. or G.v.D. (e-mail: wmbement@wisc.edu or andrew.goryachev@ed.ac.uk or DASSOW@uoregon.edu)

Received 17 February 2015; accepted 8 September 2015; published online 19 October 2015; DOI: 10.1038/ncb3251

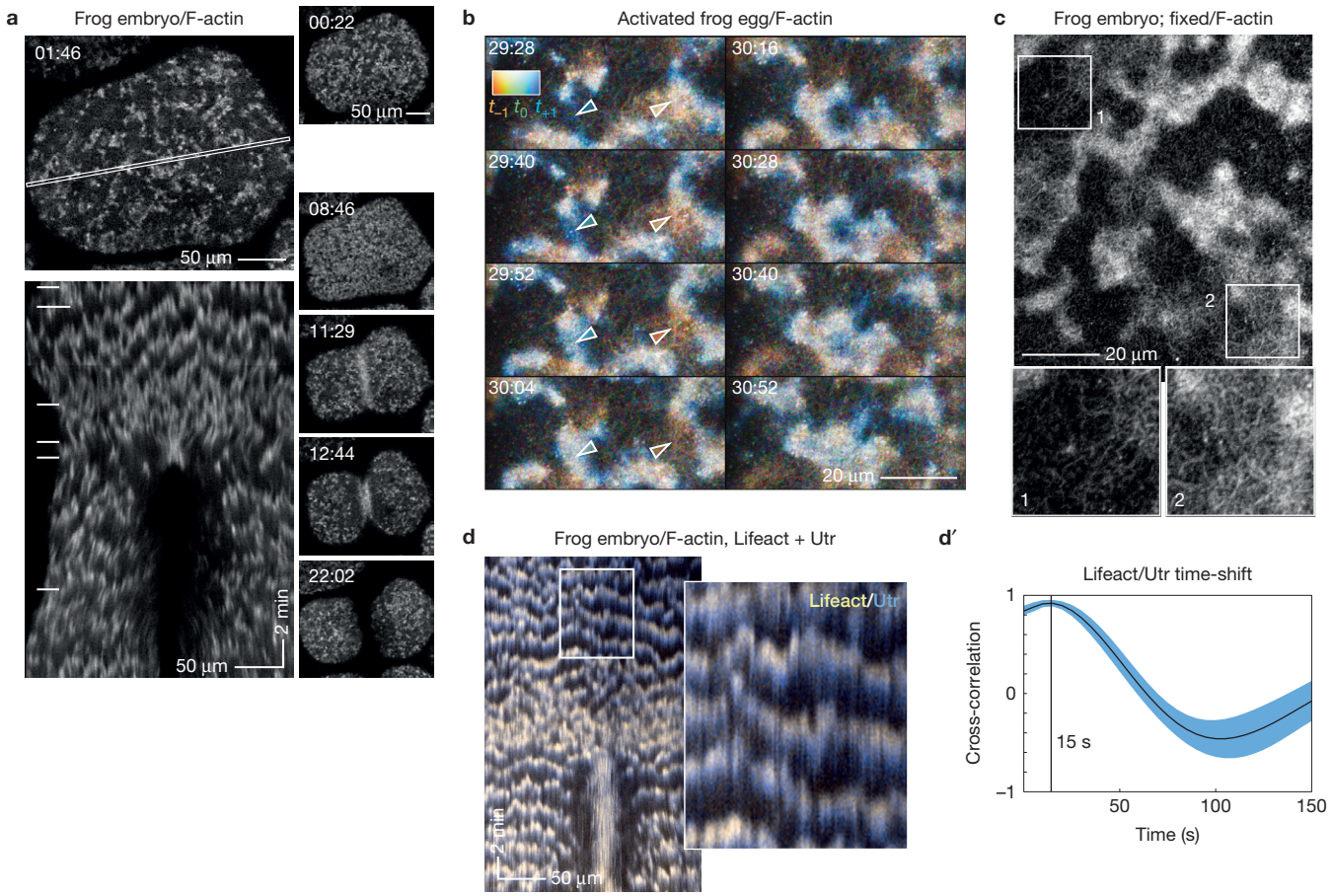

Figure 1 Cortical waves of actin assembly and disassembly in activated frog eggs and embryos. (**a**) Surface view of a frog blastomere expressing GFP–UtrCH to label F-actin. Top left: single frame; cortical F-actin consists of irregularly sized patches throughout the cortex, which, as illustrated in the kymograph made from the outlined region (bottom left) travel continually across the surface (see Supplementary Video 1). In the kymograph, F-actin waves create slanted bands with semi-regular spacing. Right: sequential frames from the same sequence throughout cytokinesis; horizontal lines in the kymograph indicate times corresponding to individual *en face* frames shown to the right. For this and all other figures, time is in min:s. (**b**) High-magnification time-lapse sequence of an activated frog egg expressing GFP–UtrCH (see Supplementary Video 2), colour coded by rendering the current frame malachite, next frame blue, last frame copper: thus, new F-actin is bluish, and old F-actin is reddish. On the left, the leading edge of the F-actin wave progresses downward while the trailing edge disappears. On the lower right, the old F-actin wave dissipates. Cables of F-actin are apparent within and between receding waves. Swatch shows colours resulting from blending RGB channels with low (bottom of swatch) to high (top of swatch) overlap. Arrowheads indicate rising (left) and falling (right) wavefronts (arrow colour sampled locally). (**c**) A fixed frog embryo stained with fluorescent phalloidin to reveal endogenous cortical F-actin; closely resembles **b**. ×2 enlarged insets (bottom) correspond to outlined areas. Inset 1 shows a region between waves; inset 2 shows a wave. Cables are present in both but are brighter and denser in the wave. (**d**) Kymograph from a time series of a frog embryo co-expressing GFP–Lifeact (yellow) and mCherry–UtrCH (blue) to label newer and older actin, respectively (see Supplementary Video 3 and Supplementary Fig. 1d); inset is a ×3 blowup. Leading edges of each wave (top of bands in kymograph) have proportionately more Lifeact and trailing edges (lower part of bands) more UtrCH, even though both probes qualitatively label the same features (Supplementary Fig. 1d). (**d′**) Cross-correlational analysis showing 15 s delay between recruitment of Lifeact and UtrCH. Images are representative of at least 40 (**a**), at least 30 (**b**), and 3 (**c**,**d**) independent experiments, respectively.

demonstrating that they are endogenous to the system. Waves traverse the cortex in an apparently random manner at $0.22 \pm 0.1\ \mu m\ s^{-1}$ (mean ± s.d.; $n = 80$ waves) with a period of 80–120 s (Fig. 1b,d and Supplementary Videos 1 and 2). Waves that were unambiguously observed to undergo collision annihilated each other (Supplementary Fig. 1d). Waves occur in artificially activated eggs, which do not cleave but otherwise mimic embryos (Fig. 1b and Supplementary Fig. 1b), but not oocytes arrested in prophase of meiosis I (Supplementary Fig. 1c).

To investigate whether the waves reflect actin assembly and disassembly, we double-labelled embryos with GFP–Utr and mCherry–Lifeact because Utr-based probes bind to F-actin slower than probes that also label G-actin, such as Lifeact[9,11]. Although both probes clearly reveal the same features (Supplementary Fig. 1d), the leading edges of waves had more Lifeact than Utr, and the trailing edges more Utr than Lifeact (Fig. 1d,d′ and Supplementary Video 3), demonstrating that the waves represent new assembly followed by disassembly, not cortical contraction or irruption from below. Further, the myosin-2 inhibitor blebbistatin[12] had no significant effect on wave period (Con = 78 ± 11 s; blebbistatin = 83 ± 8 s; mean ± s.d.; $P = 0.46$; $n = 270$ correlation curves; analysis of variance). However, by suppressing cortical contraction, blebbistatin reduced side-to-side

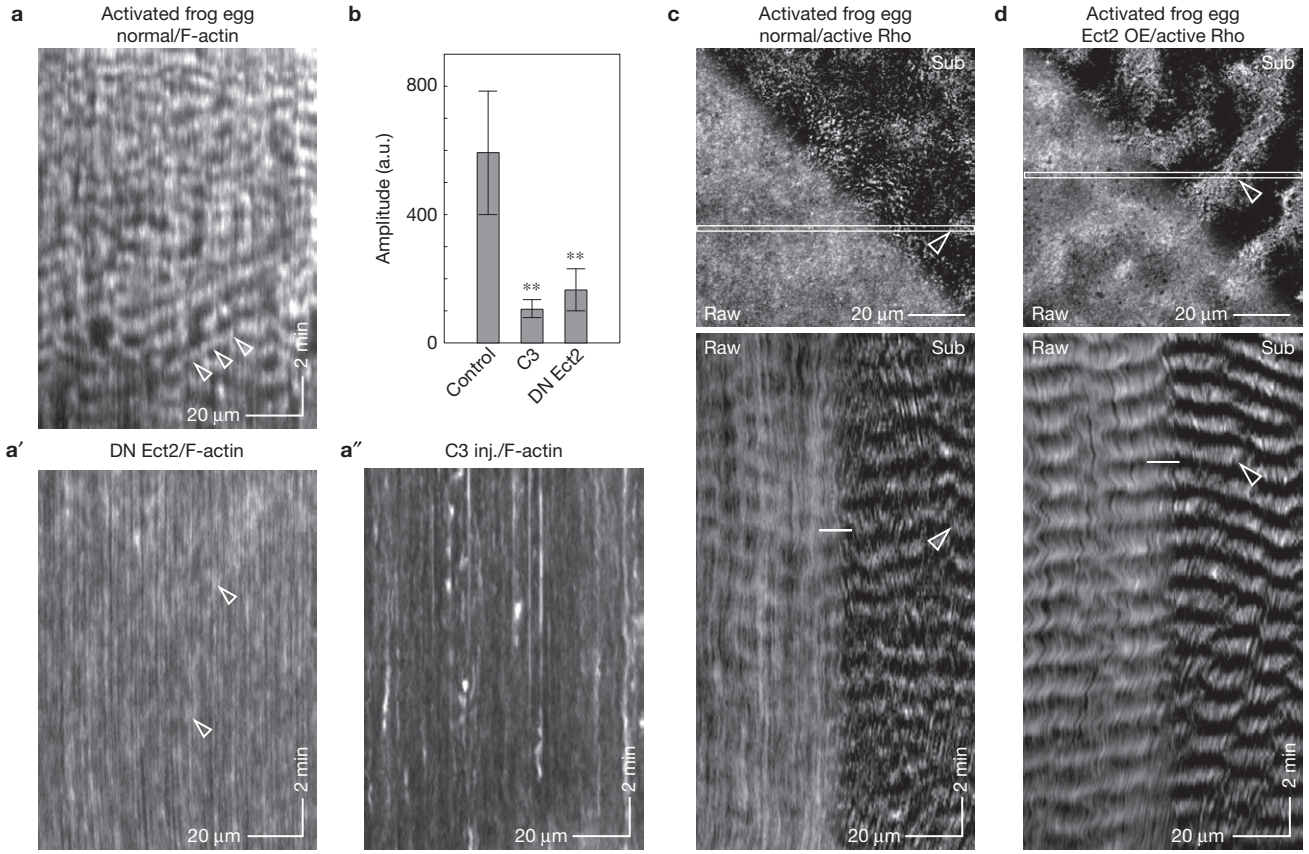

Figure 2 Cortical F-actin waves in activated frog eggs are Rho-dependent and are accompanied by Rho activity waves. (**a**) Kymograph from a control activated frog egg expressing GFP–UtrCH to label F-actin. (**a′**) Kymograph from an activated frog egg expressing GFP–UtrCH and dominant negative Ect2. (**a″**) Kymograph from an activated frog egg expressing GFP–UtrCH and C3 exotransferase to inactivate Rho. Arrowheads indicate waves. (**b**) Plot of wave amplitude in controls versus cells expressing dominant negative Ect2 or C3. Results are mean + s.d.; $n = 100$ waves; $P = 0.00012$ for C3 versus control and 0.00015 for DN Ect2 versus control; *t*-test. (**c**) Activated frog egg expressing 3×GFP–rGBD to label active Rho (see Supplementary Video 4): single frame (top) and kymograph (bottom), raw (left) and subtracted data (right, t_0–t_{-3}), highlighting rising Rho activity. The kymograph demonstrates that what otherwise looks like mundane inhomogeneity in the still image actually reflects regular waves of Rho activity; these are more evident in the processed half of both the image and kymograph. (**d**) Activated frog egg expressing 3×GFP–rGBD to label active Rho and subjected to low-level overexpression of wild-type *Xenopus* Ect2 (see Supplementary Video 5); figure processed and presented as in **c**. Waves are sharper (that is, have higher amplitude) and more continuous than normal cells (compare with **c**) and are clearly evident even without processing. **c** and **d** are derived from average projections of 4 1 µm sections at 10 s intervals. Images are representative of at least 30 (**a**), 3 (**a′**,**a″**,**b**), 4 (**c**) and 6 (**d**) independent experiments, respectively.

movement of the cortex, which permitted quantification of wave run length (maximum run length = 25 µm; mean = 3.7 µm).

Ect2 regulates cortical Rho waves in activated *Xenopus* eggs and embryos

C3 exotransferase, a specific Rho inhibitor, eliminated actin waves, but not other forms of actin assembly, such as comets (Fig. 2a″,b and Supplementary Fig. 2a). A dominant negative Ect2 (refs 2,13; the conserved GEF involved in cytokinesis) also eliminated the actin waves (Fig. 2a′,b and Supplementary Fig. 2b). We therefore sought to detect concomitant waves of cortical Rho activity. A probe for active Rho (GFP–rGBD; ref. 14) did not express quickly enough to detect any Rho patterning other than the cytokinetic Rho zone. However, Rho activity waves could be detected in activated eggs expressing 3×GFP–rGBD protein (c) or in embryos microinjected with recombinant GFP–rGBD protein (Supplementary Fig. 2c). In addition, anillin, a Rho effector protein[15], also exhibits cortical waves (Supplementary Fig. 2d) and low-level overexpression of wild-type Ect2 resulted in a striking increase in the amplitude and regularity of the Rho waves (Fig. 2d and Supplementary Fig. 2e and Supplementary Video 5).

Cortical Rho waves in starfish oocytes and embryos

In parallel experiments we discovered that *Patiria miniata* (starfish) oocytes and embryos exhibit cortical Rho activity waves that, in contrast to frog, are clearly visible only during a ~10–15 min window post-anaphase. At anaphase of meiosis I, Rho activity spread from the vegetal pole towards the animal pole, culminating in polar body emission (Fig. 3a and Supplementary Video 6). Low-level overexpression of wild-type Ect2 profoundly amplified meiotic Rho activity and extended its duration, producing extremely regular, persistent (maximum run length = 55.8 µm; mean = 6.5 µm), high-amplitude waves kinematically similar to those in frogs, including overtly spiral repeating patterns (Fig. 3b,c and Supplementary Video 7). Higher-magnification videos of normal starfish oocytes

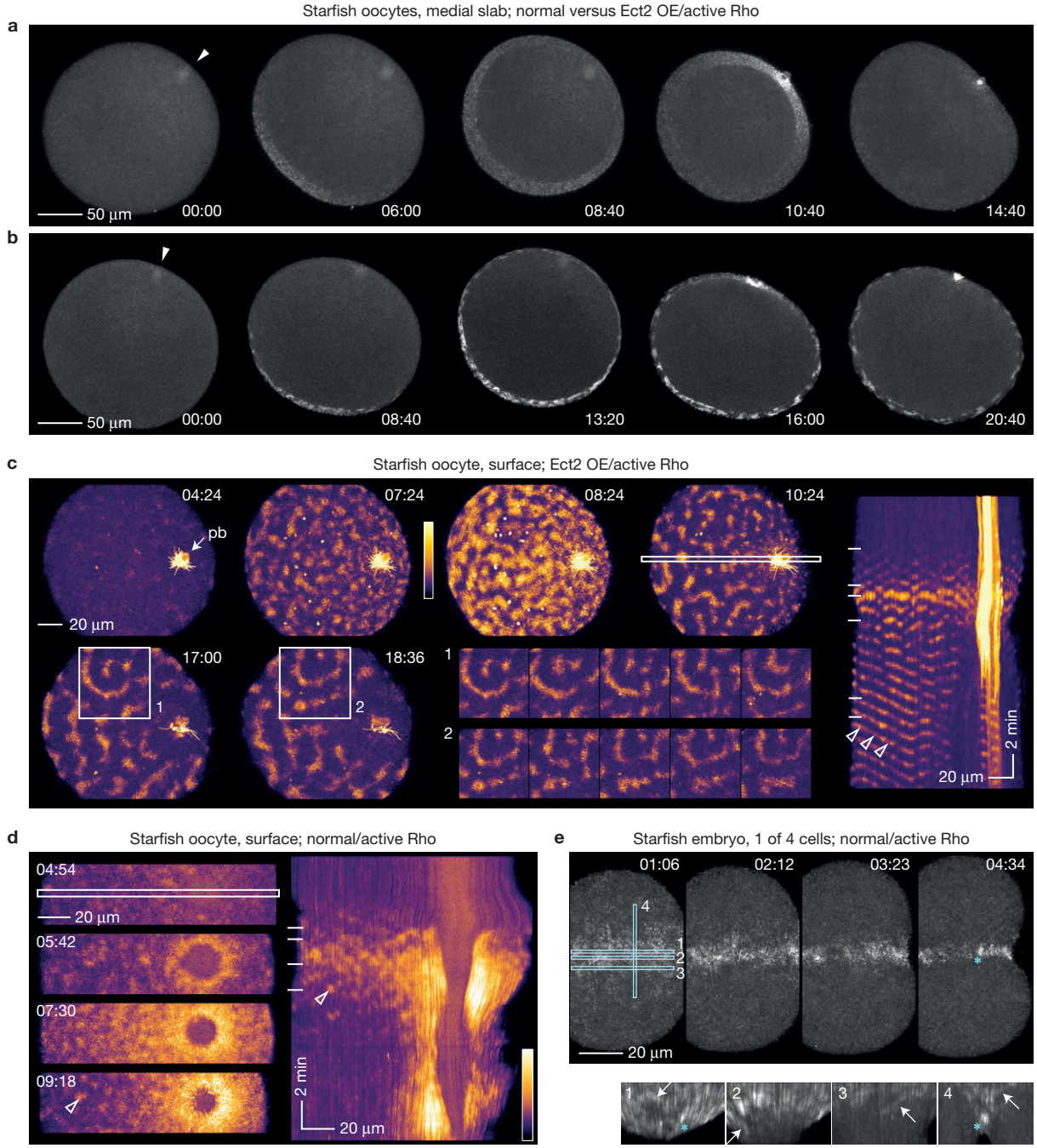

Figure 3 Rho activity waves in starfish oocytes and embryos. (**a**,**b**) Frames from time-lapse sequences of Rho activity during meiosis I in a normal starfish oocyte (top; projection of 8 1 μm sections) and an oocyte overexpressing wild-type *Strongylocentrotus purpuratus* Ect2 (bottom; projection of 8 1.5 μm sections). See Supplementary Video 6. Arrowhead indicates animal pole. Rho activity appears at the vegetal pole, spreads upward, and converges on the nascent polar body, forming a cytokinetic Rho zone. In Ect2-expressing oocytes the global pattern of Rho activity mirrors that of controls but waves are much brighter, travel further, and persist after polar body emission. (**c**) Surface view of cortical Rho activity in a meiosis II oocyte overexpressing Ect2 (see Supplementary Video 7; pb, polar body; projection of 14 1 μm sections). High-amplitude waves form and settle into repetitive, often spiral, patterns. Inset montages are successive 60 s time points from the outlined region on the left starting at 17:00 (1) or 18:36 (2), showing patterns that approximately replicate on a ~70 s timescale (1 is spiral, 2 is centre-surround with a slash underneath). Kymograph on the right was generated from the area indicated by the outlined strip, fourth frame. Diagonal bands span half the oocyte, showing that waves travel at least this far. Horizontal lines in the kymograph mark times of frames shown on the left. Arrowheads point to a wavefront that traverses tens of micrometres at a steady speed. (**d**) Surface view of cortical Rho activity in a normal starfish oocyte; single frames (left) and kymograph (right). Rho waves appear, brighten, and coalesce into a continuous zone around the nascent polar body (see Supplementary Video 8). Arrowheads indicate a wavelet that appears in both the kymograph and the still frame. (**e**) Rho activity in a normal starfish blastomere (1 of 4 cells); still frames and kymographs generated from the strips outlined in blue: 1, furrow centre; 2, furrow periphery; 3, just outside furrow; 4, across furrow. Rho waves focus at the equator before ingression, appear in the furrow (arrows), and eventually merge into a coherent Rho zone. Asterisk indicates a particularly bright focus that appears in the fourth still frame and kymographs 1 and 4. Images are representative of 10 (**a**,**d**), 20 (**b**,**c**) and 4 (**e**) independent experiments, respectively.

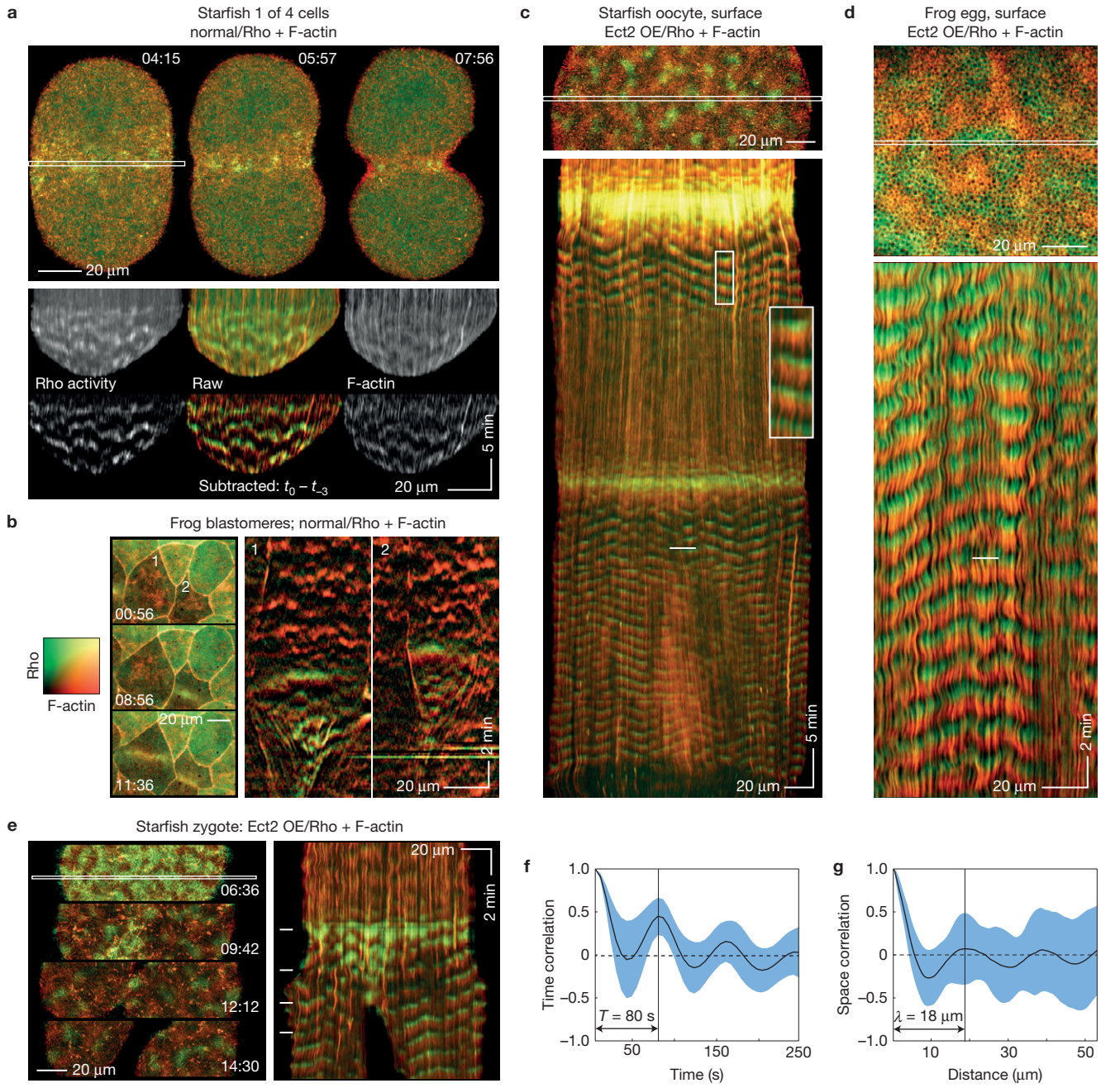

Figure 4 F-actin assembly fronts directly follow, but overlap minimally with, Rho activity waves. The colour table in **b** applies to all images in this figure. (**a**) A normal starfish blastomere co-expressing GFP–rGBD (malachite; Rho activity) and GFP–Utr (copper; F-actin); selected frames (top) from a time-lapse sequence of cytokinesis (Supplementary Video 9), and raw and subtracted kymographs (bottom) made from the outlined strip. In the still images, the cytokinetic furrow is populated by apparently random densities of active Rho and F-actin; kymographs show these correspond to wavelets in which Rho activity rises, and then falls as actin assembles. (**b**) Still images (left) and kymographs (right) from a time-lapse video of cortical F-actin and Rho activity in a frog embryo showing two cells (1, 2) undergoing cytokinesis. Rho waves in the furrow are followed by F-actin assembly waves. (**c**) Rho activity and F-actin in a starfish oocyte modestly overexpressing wild-type Ect2; kymograph (bottom) made from the strip outlined in the still frame (top). See Supplementary Video 10. Except during the global burst of Rho activity accompanying each meiotic cytokinesis, Rho activity waves immediately precede F-actin assembly, and F-actin disassembly precedes each Rho activation wave. Inset magnifies four cycles from the wave train after the first meiosis, emphasizing the minimal overlap (yellow) between malachite and copper, and the dark zone separating copper from the next malachite wave. (**d**) An activated frog egg subjected to Ect2 overexpression; probes and presentation as in **c** (see Supplementary Video 11). Although waves are more tightly packed in frog eggs, kymographs show a strikingly similar relationship between Rho and actin waves as in normal starfish. (**e**) A starfish zygote overexpressing Ect2 (see Supplementary Video 12); probes and presentation as in **c** and **d**; positions of still frames (left) are indicated by dashes in the kymograph (right). Faint waves precede the global rise in Rho activity that focuses equatorially, leaving lower-amplitude waves in non-furrow regions; throughout, F-actin assembly follows peak Rho activity, and dark phases precede each Rho wave. (**f**) Temporal correlation plot of Rho waves from starfish oocytes overexpressing Ect2. Wave period ~80 s. (**g**) Spatial correlation plot of Rho waves from starfish oocytes overexpressing Ect2. Wavelength 18 µm. Images are representative of 4 (**a**,**b**) 8 (**c**), or 5 (**d**) independent experiments, respectively.

(that is, oocytes not subject to Ect2 overexpression) showed that much of the meiotic Rho activity comprised low-amplitude, rapidly damped cortical waves (Fig. 3d and Supplementary Video 8). Rho activity subsided before onset of meiosis II, reappeared coincident with anaphase of meiosis II, again spreading from the vegetal to the animal pole, and culminated in polar body emission (not shown). In the largest mitotic cells, waves of cortical Rho activity also formed at anaphase onset, but were rapidly lost from polar regions and instead were confined to the equatorial cortex (Fig. 3e and Supplementary Fig. 3a,b). Waves initially dominated the furrow region itself, but as the furrow ingressed, relatively stable patches of Rho activity eventually merged into a coherent cytokinetic Rho zone (Fig. 3e and Supplementary Fig. 3b–d). As cells decreased in size, the time window in which polar waves were apparent after anaphase onset became narrower, as did the prominence of waves in the furrow itself (Supplementary Fig. 3c,d).

Spatio-temporal coordination of Rho and actin waves

Simultaneous imaging of active Rho and F-actin within the cleavage furrow of control starfish zygotes and frog blastomeres revealed another surprise: instead of overlapping, F-actin assembly fronts directly follow Rho activity waves (Fig. 4a,b and Supplementary Video 9). The same pattern (high-amplitude Rho waves followed by F-actin waves) was triggered globally in both activated frog eggs and starfish oocytes or mitotic cells by Ect2 overexpression (Fig. 4c–e and Supplementary Videos 10–12). In all cases (except once waves cede to coherent zones, for example, in progressing furrows) peak actin assembly coincides spatially with decreasing Rho activity, and a latent period with relatively low cortical Rho and actin follows each cycle. Although superficially similar to calcium waves that develop following expression of exogenous neurotransmitter receptors[16], the Rho and actin waves are ∼10 times slower than calcium waves and are not associated with elevated calcium (not shown).

To quantitatively characterize the wave pattern, we performed spatial and temporal autocorrelation analyses[17,18]. These analyses demonstrated that in starfish oocytes both Rho and actin waves had a wavelength of 18 μm and propagated with the same velocity, ∼0.225 μm s^{-1} (Fig. 4f,g). In activated frog eggs, the waves were slower, ∼0.18 μm s^{-1}, and longer, ∼21 μm. Importantly, analysis of the cross-correlation between Rho and F-actin signals showed that F-actin waves followed Rho with a fixed delay, 18 s in starfish and 48 s in frog. Thus, Rho and F-actin waves are mutually coordinated parts of the same wave pattern. Furthermore, such a constant time delay suggests that F-actin might effectively suppress Rho activation.

Rho–actin waves represent cortical excitability leading to spiral turbulence

Propagating waves that undergo self-annihilation on collision suggest excitable dynamics[19]. Excitable media generate waves that travel without damping because they are generated *de novo* by rapid local autoactivation at their front and extinguished at their wake by delayed negative feedback. Rho is a good candidate for the activator as small GTPases can indirectly activate themselves autocatalytically[20]. On the basis of our kinematic observations, F-actin seemed a promising candidate for negative feedback. To test this possibility, we exploited the fact that quantitative relationships between Rho and F-actin can be directly inferred from imaging data[17] (see Methods). In cortical loci (image pixels) with low F-actin signal, the rate of Rho signal change and the value of Rho signal itself are statistically positively correlated (Fig. 5a). As F-actin concentration is low at the front of the excitable wave, this correlation implies that, at the wavefront, Rho amplifies itself in a positive feedback loop, which is the required property of the activator. Likewise, F-actin assembly positively correlates with Rho activity at the wavefront (Fig. 5b), and Rho activity negatively correlates with F-actin accumulation at the wave back (Fig. 5c). We already established that Rho activity is required for actin assembly waves and that amplifying Rho activity elicits excess actin assembly; the correlative image analysis, thus, quantitatively confirms the dynamic relationship expected for the activator–inhibitor coupling (see Supplementary Fig. 4a–c).

What factors shape the wave patterns? Random fluctuations in F-actin density and concentrations of other proteins are necessary to induce dynamics in excitable cellular systems[19]. However, occasionally visible fragments of spiral waves (Fig. 3c and Supplementary Videos 7, 10 and 11) suggest an underlying behaviour much more complex than simply uncorrelated spatio-temporal noise. To reveal it, we reconstructed the phase of the excitable dynamics using a recently developed procedure[21] (Fig. 5d–f and Methods). This approach revealed multiple spiral waves (normally obscured by noise) whose cores spontaneously emerge, erratically move and disappear generating spiral wave turbulence. Although most spiral cores were very short lived (a few seconds), some persisted for up to ∼59 min (Supplementary Video 13), reminiscent of the self-sustained spiral waves that emerge from the ends of broken wavefronts of cardiac excitation and cause atrial fibrillation in the heart[22].

Antagonism of Rho by F-actin

The excitability model predicts that restricting F-actin assembly would extend the rising phase of Rho activation, resulting in waves with higher amplitude and crest widths. Treatment of starfish oocytes overexpressing Ect2 with latrunculin B to reduce F-actin caused global collapse of cortical F-actin and increased Rho activity (Supplementary Fig. 5a); conversely, treatment with jasplakinolide to stabilize F-actin attenuated Rho waves (Supplementary Fig. 4e,e′). Local F-actin disruption by means of latrunculin B-filled microneedles positioned near the cell surface was more informative: high needle concentrations (>5 μM) of latrunculin caused rapid local dissolution of cortical actin and a parallel burst of Rho activity (Fig. 5g and Supplementary Video 14), which tapered off after the entire cortical actin network dissolved. Lower concentrations (1–0.5 μM; Fig. 5h and Supplementary Video 15), or greater distance from the needle (Fig. 5g, lower cell), resulted in slower loss of cortical F-actin and a corresponding amplification of Rho wave amplitude and crest width. Importantly, when applied at concentrations that permitted some residual actin assembly to cells with active waves, latrunculin induced a sustained shift to higher wave amplitude and longer period (Fig. 5h). Similar results, albeit less pronounced, were observed in latrunculin-treated normal cells (Supplementary Fig. 5). This directly confirms that F-actin assembly somehow suppresses Rho activation, supporting a model of cortical excitability in which F-actin-dependent Rho inhibition represents the essential negative feedback.

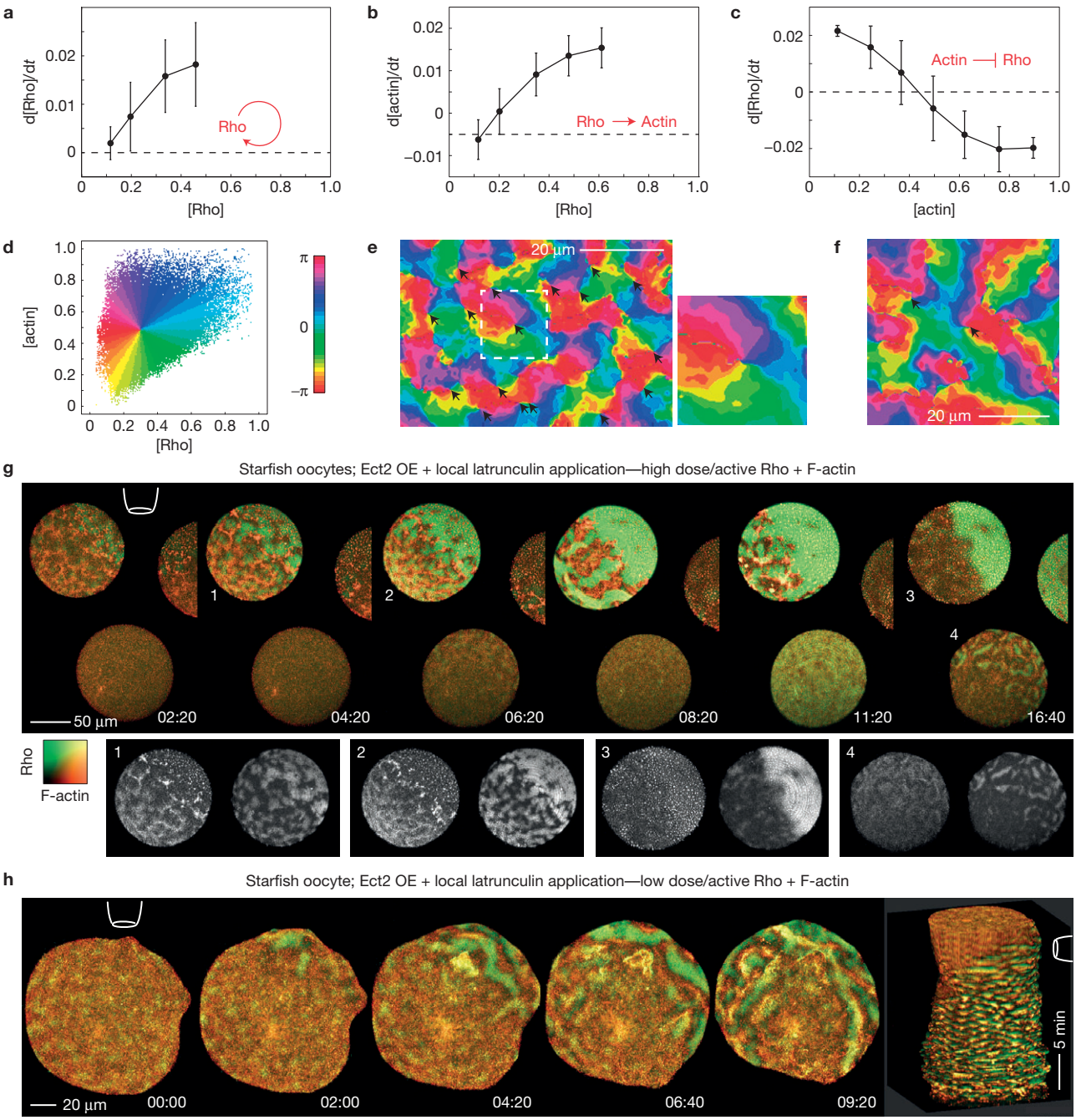

Figure 5 Analysis of Rho and F-actin dynamics reveals cortical excitability and spiral turbulence. (**a**) The Rho activation rate (mean ± s.d.) increases with Rho activity signal indicating that Rho activates itself in a positive feedback loop. Correlation assessed from pixels with low F-actin signal (see Supplementary Fig. 4a). (**b**) The F-actin accumulation rate is positively correlated with Rho activity (assessed from pixels with low F-actin signal). (**c**) The Rho activation rate is inversely correlated with F-actin signal, to the point of switching to inactivation at high F-actin density (assessed from pixels with high Rho activity signal). Results are mean + s.d.; $n=900$ cycles. (**d**) Each cortical locus (image pixel) can be mapped by its particular values of Rho activity and F-actin density to a single phase value, an angle between 0 and 2π, shown in rainbow colours: Cortical loci at the front of waves appear green, loci at Rho wave crests as cyan, at F-actin wave crests as dark blue–magenta, and loci at the back of the wave are red and orange. (**e**) Phase reconstruction for a starfish oocyte overexpressing Ect2 (Supplementary Video 13). Points where all rainbow colours (phase values) merge indicate spiral cores (arrows). Inset: magnification of spiral wave core neighbourhood outlined by the dashed line. (**f**) Phase reconstruction for an activated frog egg overexpressing Ect2. (**g**) Meiotic Ect2-overexpressing starfish zygotes containing GFP–rGBD (Rho activity; malachite) and mCherry–Utr (F-actin; copper); time-lapse sequence after application of a high concentration of latrunculin B (10 µM) from an agarose-filled pipette (position indicated by cartoon); treatment causes rapid cortical F-actin collapse and a corresponding burst of Rho activation (see Supplementary Video 14). Insets: single-channel images of cells/stages indicated by numerals: (1) initial response, (2) wave regime on far side, collapse on near side, (3) total collapse, (4) wave regime on near side of distant oocyte. (**h**) Similar to **g**, but low-dose (1 µM) latrunculin B induces a shift from the typical Ect2-enhanced wave regime to a higher-amplitude, longer-period wave regime, in which large-scale Rho waves propagate away from the site of local F-actin disassembly (see Supplementary Video 15); rightmost image is a kymocube rendered using ImageJ. Images are representative of 5 independent experiments.

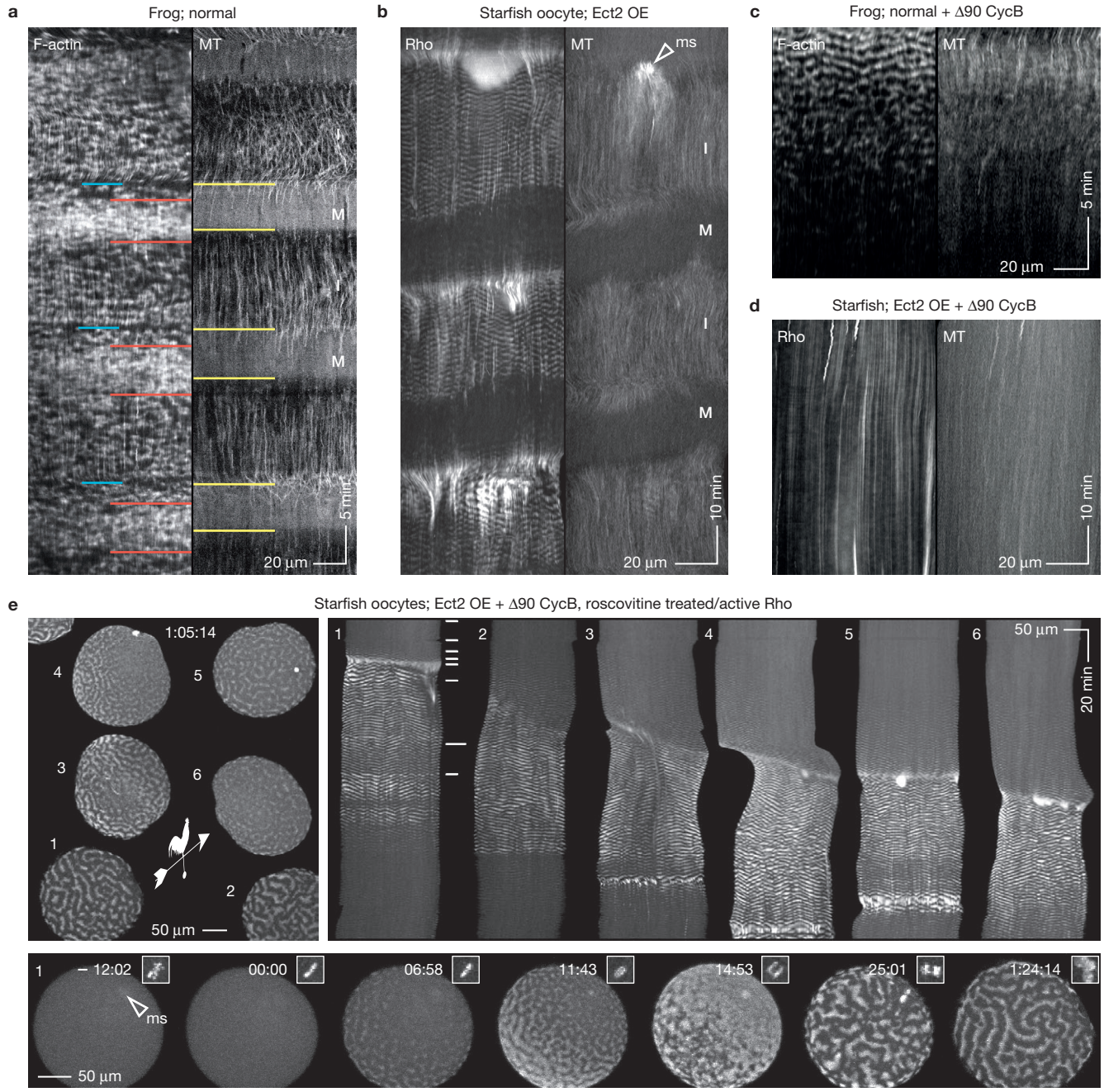

Figure 6 Cdk1 gates excitability. (**a**) Kymograph from a normal frog embryo showing waves of cortical F-actin (left) and cortical microtubules (right). I, interphase; M, M-phase; yellow lines on right indicate M-phase onset, as revealed by loss of cortical microtubules. Actin waves persist throughout M-phase but wave density varies: at M-phase onset (blue line on left), waves are spaced farther apart; this is followed by a period of the same length as M-phase but slightly delayed in which F-actin waves are brighter (red lines). (**b**) Kymograph from a double-labelled starfish oocyte overexpressing Ect2 showing waves of cortical Rho activity (left) and cortical microtubules (right). Rho waves cease in each M-phase and reappear in each interphase. ms, meiotic spindle. (**c**) Kymograph of a frog blastomere expressing Δ90 cyclin B showing cortical F-actin (left) and cortical microtubules (right). As the time of high Cdk1 activity lengthens (revealed by loss of cortical microtubules) cortical F-actin waves progressively disappear. (**d**) Kymograph of an Ect2-overexpressing starfish oocyte expressing Δ90 cyclin B as well, showing cortical Rho activity (left) and cortical microtubules (right). Rho waves fail to appear as the cell remains arrested with high Cdk1 activity. (**e**) Top left: Rho activity in starfish oocytes overexpressing Ect2 and expressing Δ90 cyclin B, 65 min after treatment with 40 µM roscovitine to inhibit Cdk1 (see Supplementary Video 16). The weather vane indicates the direction of roscovitine flow. Roscovitine-containing sea water perfused around tight-packed oocytes from southeast to northwest at time 00:00; cells 1 and 2 are at the cluster edge, and cells 5 and 6 are in the cluster centre; hence, the weathervane indicates the presumed gradient of drug exposure. All oocytes show robust Rho waves at this time point. Top right: kymographs of oocytes (identified by numerals) showing development of cortical Rho activity waves following roscovitine treatment. Note that the onset of waving follows the expected rate of Cdk1 inhibition based on access to drug in perfused media. Bottom: successive frames showing oocyte 1 alone; inset shows chromosomes, and arrowhead indicates position of meiotic spindle. Rho waves are well developed at least five minutes before anaphase begins. Images are representative of 4 (**a**), 3 (**b**), 5 (**c**) and 6 (**d**) independent experiments, respectively.

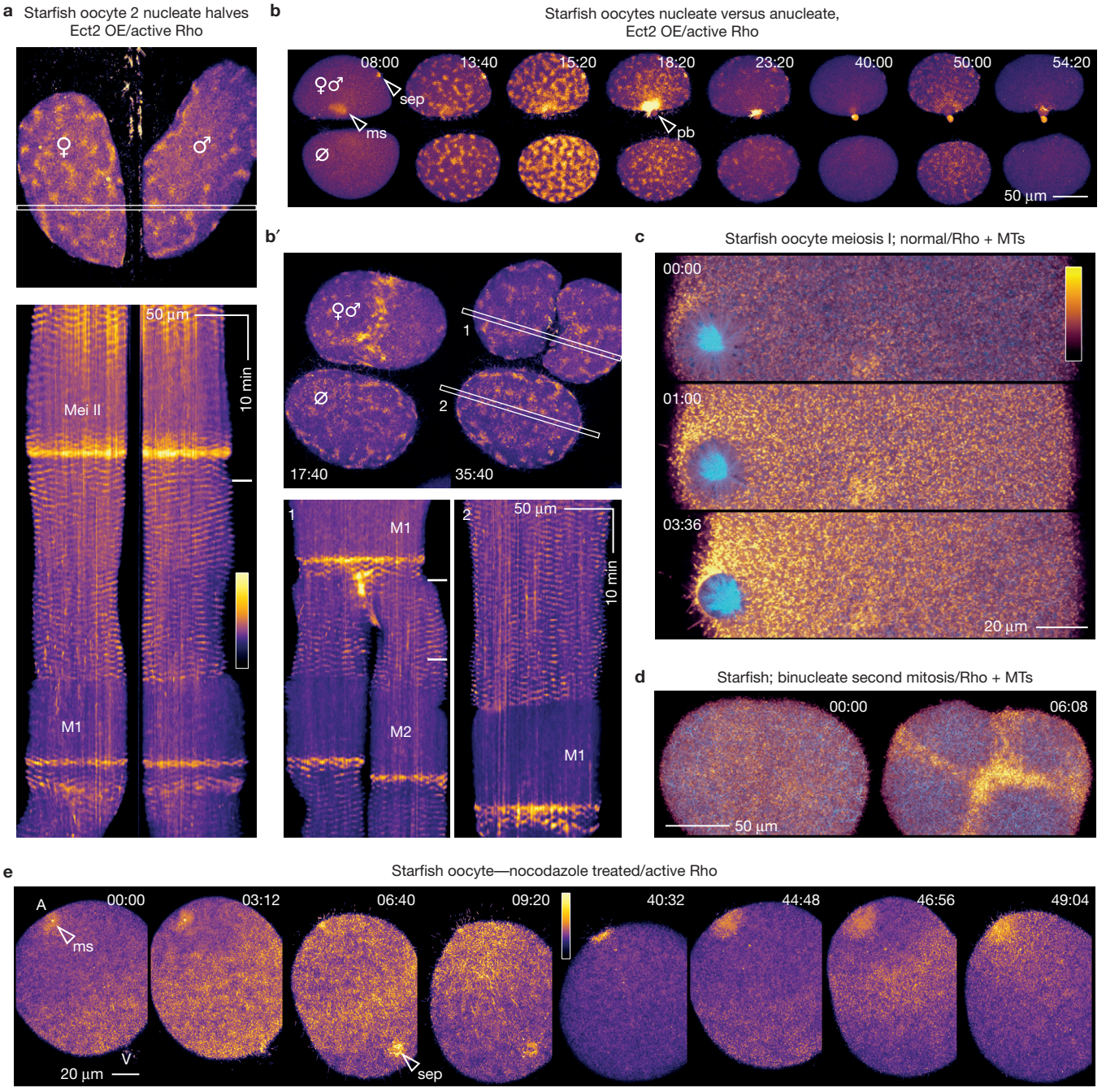

Figure 7 Excitability does not require spindles but is locally modulated by microtubules. (**a**) Still frame (top) and kymograph (bottom) from a time-lapse video showing cortical Rho activity in two nucleate fragments derived from bisection of an Ect2-overexpressing starfish oocyte. Waves of Rho activity appear and disappear in synchrony in each half. The pseudocolour table shown applies to **a**,**b**,**b**′, and **e**; in **a** and **b**′, the outlined strips indicate the kymograph region, and the dashes in the kymographs are times of the still frames. (**b**) Frames from a time-lapse video showing cortical Rho activity in the nucleate half (top) and the anucleate cytoplast (bottom) after bisection of an Ect2-overexpressing starfish oocyte just before meiosis I. Waves appear and disappear on time in the anucleate cytoplast in spite of the fact that it lacks a spindle, chromosomes, or even centrosomes (see Supplementary Video 17). (**b**′) Similar bisection but after meiosis; two frames (top), during and after the first cleavage, and kymographs (bottom, 1: nucleated, 2: anucleate). Cortical Rho waves appear and disappear in both halves, although the first mitosis is delayed in the anucleate cytoplast. (**c**) Frames from a time-lapse video showing microtubules (cyan) and active Rho (gold) in a normal starfish oocyte during meiosis I. Rho activity is suppressed in the region occupied by the spindle aster. (**d**) Frames from a time-lapse video showing microtubules (cyan) and active Rho (gold) in a starfish zygote with two spindles. Rho activity waves are excluded from regions occupied by spindle asters leading to focusing of Rho waves into a cruciform Rho zone. (**e**) Meiotic Rho activity in a normal starfish oocyte after treatment with 5 µM nocodazole to depolymerize microtubules (see Supplementary Video 18). The overall pattern of Rho activation is similar to controls—initiation at the vegetal end, rapid progression to the animal pole, inactivation in M-phase—except that the animal pole is a Rho hotspot instead of a suppressed area; sep, sperm entry point, ms, meiotic spindle. Images are representative of 3 (**a**,**b**), 12 (**c**), 17 (**d**) and 3 (**e**) independent experiments, respectively.

Cdk1-dependent control of excitability

To better characterize the relationship between cell cycle progression and excitability, cortical microtubules were used as a marker for cell cycle progression[23] and compared with either cortical F-actin (frogs) or cortical Rho (starfish). Cortical microtubule abundance changed rhythmically with the cell cycle in frog embryos, with high levels in interphase and very low levels in M-phase, but cortical actin waves were present throughout (Fig. 6a). However, in starfish oocytes or embryonic cells overexpressing Ect2, cortical Rho waves were evident for ~63% of the cell cycle, disappearing and appearing in concert with cortical microtubules (Fig. 6b). In control cells, Rho waves were normally visible for ~20% of the cell cycle (not shown).

As M-phase results from activation of cyclin-dependent kinase 1 (Cdk1), we microinjected cells with messenger RNA encoding Δ90 cyclin B, which prevents Cdk1 inactivation[24]. In frogs, this resulted in progressive disappearance of actin waves coincident with complete disappearance of cortical microtubules (Fig. 6c). Similarly, in starfish, Δ90 cyclin B produced an indefinite cessation of Rho waves (Fig. 6d). Thus, Cdk1 activity suppresses excitability in both systems. To determine whether Cdk1 inactivation initiates excitability, Ect2-overexpressing starfish oocytes were microinjected with Δ90 cyclin B mRNA, and subsequently treated with roscovitine to inhibit Cdk1 (ref. 25). Roscovitine treatment triggered reappearance of cortical Rho waves in a manner that paralleled the expected exposure to the drug (Fig. 6e and Supplementary Video 16). Moreover, simultaneous imaging of active Rho and fluorescent histone demonstrated that roscovitine treatment actually released Rho waves even before anaphase onset (Fig. 6e and Supplementary Video 16). Thus, Cdk1 inactivation is indeed a trigger of excitability.

DNA, centrosomes, microtubules and excitability

C-phase onset and cessation are regulated independently of the spindle[6]. To determine whether excitability is likewise spindle-independent, starfish oocytes overexpressing Ect2 were microdissected to produce pairs of cytoplasts that contain or lack essential spindle components—DNA and centrosomes[23]. Cytoplasts that contained neither DNA nor centrosomes nonetheless exhibited excitability (Fig. 7b and Supplementary Video 17), and the timing and character of waves were remarkably similar to those of nucleated cytoplasts or whole cells (Fig. 7a,b), with the exception of a long delay between meiosis and the first mitosis in anucleates (Fig. 7b′). Thus, neither DNA, nor nuclei, nor spindles are required for temporal regulation of excitability.

Although the temporal regulation of C-phase is independent of microtubules, microtubules nevertheless spatially regulate cortical contractility during C-phase[6]. Simultaneous imaging of microtubules and Rho activity in starfish oocytes and embryos illustrates that excitability is subject to spatial regulation by microtubules, as expected for a manifestation of C-phase: Rho waves were suppressed in regions where astral microtubules densely populate the cortex (Fig. 7c,d). Further, microtubule disassembly by nocodazole prevented formation of the wave-free region at the animal pole in oocytes (Fig. 7e and Supplementary Video 18) but had no apparent effect on the timing of wave appearance or disappearance (Fig. 7e), indicating that, although microtubules do not control the timing of excitability, they are nonetheless responsible for locally modulating it.

A model for cortical excitability suggests the route to furrow formation

To better understand cortical excitability, we developed a simple model (Fig. 8a,b) that incorporates membrane–cytoplasmic shuttling of inactive Rho, its Ect2-dependent autocatalytic activation and its inactivation via a slower, F-actin-mediated negative feedback (see Methods). The spatio-temporal excitable dynamics of the model driven by molecular noise (Fig. 8 and Supplementary Fig. 6b,c) faithfully recapitulates the pattern of spontaneously emerging, erratically moving and colliding waves. Moreover, the wave pattern and kymograph signature of the global wave-like rise in Rho activity observed during meiosis are captured by the model simply by including a transient peak in Ect2 activity (Fig. 8c–e and Supplementary Fig. 6b,c and Supplementary Video 19), suggesting that the overall increase in Rho activity and specific changes in the wave pattern following anaphase onset reflect the rise in Ect2 activity.

We further questioned whether the transition of mitotic cells from uniform wave dynamics to equatorially focused waves could reflect microtubule-mediated redistribution of Ect2 towards the cell equator. Indeed, model simulations demonstrated a transition from a weak global excitability to progressively narrower and more intense excitability at the equator (Fig. 8f,f′ and Supplementary Video 20). Driving Ect2 localization to an even narrower band with higher local concentration caused the model to transition from excitability to a new steady state in which both Rho activity and F-actin density are high and stable, which corresponds to the behaviour observed in mature ingressing furrows. Excitable dynamics could still be visible on furrow margins where Ect2 concentration sharply drops, just as seen *in vivo* (Figs 3e and 4a). Finally, we modelled the consequences of rapid microtubule depolymerization on the established cytokinetic zone. This produced a rapid loss of high excitability from the furrow and re-emergence of weaker excitability elsewhere (Fig. 8g,g′). This model prediction was tested by treating Ect2-overexpressing starfish zygotes with nocodazole after the formation of the cytokinetic Rho zone. This completely reversed the sequence of events seen in wild-type cells: the furrow disassembled and waves reappeared throughout the cell cortex (Fig. 8h and Supplementary Video 21), in close agreement with model simulations.

DISCUSSION

We have discovered that the cortex of vertebrate and invertebrate oocytes and embryos is an excitable medium, which is based on Rho autoactivation and F-actin-mediated Rho inhibition (Fig. 8). Positive feedback (Rho autoactivation) would allow the cortex to respond to spindles experimentally deprived of astral or midzone microtubules[23] via auto-amplification at the cortex. Conversely, the negative feedback (F-actin-mediated Rho inhibition) would efface established Rho zones and cytokinetic apparatuses on repositioning of the spindle[4,26,27]. Thus, excitability explains both the sensitivity of the cortex to spindle-generated signals and the rapid adaptation of the cortex to changes in spindle position.

The relationship between cortical excitability and the cell cycle, together with the fact that cytokinesis ensues when excitability becomes confined to the equator, provides a simple explanation for C-phase: it represents the period of the cell cycle in which cortical excitability is fully enabled. Consistent with this proposal, it has been

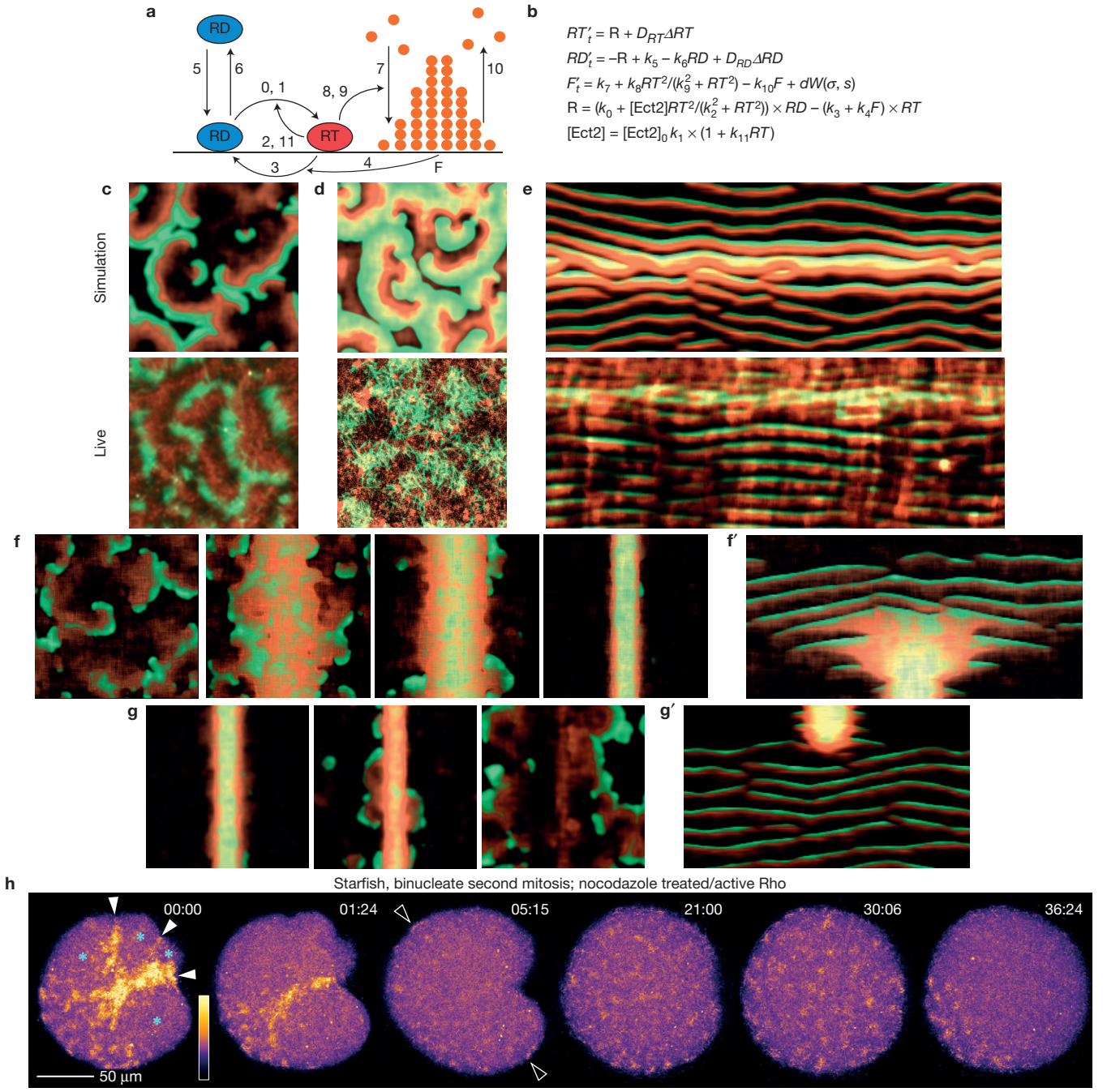

Figure 8 Model of excitable dynamics predicts that Ect2 spatio-temporal distribution determines the pattern of Rho–actin cortical activity. (**a**) Schematic diagram of the molecular processes described by the model (see Methods). Numbers on the arrows correspond to numbers of rate constants in **b**. (**b**) Model equations (see Supplementary Fig. 6a and Methods). (**c**) Top: simulation of wave turbulence with the Ect2 level representing the interphase wave pattern in starfish oocytes with extra Ect2 (see Supplementary Video 19), active Rho (malachite) and F-actin (copper). Bottom: image of cortical Rho (malachite) and F-actin (copper) from an Ect2-overexpressing starfish oocyte for comparison. (**d**) Top: model dynamics at the peak of global Ect2 activity—representing the polar body emission phase—demonstrates a characteristic wave pattern with broad crests, substantial overlap of Rho and F-actin maxima and narrow refractory zones between wave crests (see also Supplementary Fig. 6b,c and Methods). Bottom: image of cortical Rho (malachite) and F-actin (copper) from an Ect2-overexpressing oocyte at the time of polar body emission for comparison. (**e**) Top: model kymograph of Rho activity and F-actin before, during and after polar body emission (see Supplementary Video 19). Bottom: experimental kymograph for comparison. (**f**) Emergence of a furrow through condensation of waves in a simulation representing mitotic starfish cells with progressive focusing of Ect2 at the cell equator (see Supplementary Video 20). (**f′**) Kymograph along a line perpendicular to the furrow for the model behaviour in **f**. (**g**) Simulation of rapid microtubule depolymerization after furrow zone formation: the furrow signal dissipates and spatially homogeneous waves return. (**g′**) Kymograph of the simulation shown in **f**. (**h**) Behaviour of cortical Rho waves following experimental microtubule depolymerization by nocodazole in a binucleate starfish zygote at the onset of cytokinesis. Cytokinetic Rho zones dissipate quickly and waves repopulate the entire cortex. Asterisks indicate spindle pole positions; filled arrowheads indicate Rho zones in nascent furrows; open arrowheads point out instances of cortical Rho waves in once-bare territory (see Supplementary Video 21). Images in **h** are representative of 3 independent experiments.

shown that furrowing in sand dollar zygotes normally occupies about 20% of the cell cycle but can be extended to ~60% by manipulation of spindle position[4], closely paralleling our observation that Rho waves are normally evident for about 20% of the cell cycle but can be extended to about ~60% by overexpression of Ect2. Further, early frog blastomeres exhibit continuous excitability consistent with the observation that C-phase of one cell cycle overlaps with C-phase of the next cell cycle such that multiple furrows may be found in a single cell[4].

How, exactly, is excitability regulated? The results point clearly to Cdk1. Not only does cessation of excitability in starfish oocytes and zygotes coincide precisely with the onset of M-phase, waves are stripped from the cortex in an animal-to-vegetal pole manner, following the known spatial pattern of Cdk1 activation[28,29]. Further, suppression of Cdk1 inactivation arrests cells in a non-excitable state, which is rapidly converted to excitable by experimental inhibition of Cdk1. Thus, excitability in echinoderms is negatively regulated by Cdk1 and it is extremely likely that the characteristic top-to-bottom stripping of the waves from the cortex reflects the underlying 'trigger wave' of Cdk1 activation[30]. Ect2 is a potential target of Cdk1 in this context, in that Cdk1 phosphorylation compromises the ability of Ect2 to bind the plasma membrane[13]. Why waves are not fully suppressed in M-phase in frogs remains to be seen, but on the basis of the demonstration that these cells are metachronous[28,31] and the fact that they do terminate wave activity when forced into a prolonged M-phase, we speculate that their normal Cdk1 activity levels fail to reach the threshold needed to suppress excitability.

The F-actin-mediated antagonism of Rho activity observed here seems counterintuitive to the point of deviance given traditional views on collaboration of Rho and F-actin in contractile arrays. However, at least two parallels are found in other processes. During single-cell wound repair, a ring-like wave of Rho activity forms in a region of low cortical F-actin density[32]; as the Rho wave closes, it is 'chased' inward by a surrounding, ring-like wave of F-actin. Similarly, during blebbing, it is thought that Rho activity rapidly rises in regions of the cortex from which F-actin is cleared, and as Rho activity falls, F-actin rises[33–35]. Further, although not yet directly demonstrated, negative feedback from F-actin to Rho family GTPases explains essential features of cell locomotion-associated F-actin waves[36,37].

Finally, two other striking points emerge from this study. First, the fact that furrowing commences as overlapping waves of Rho activity and F-actin become confined to the equator suggests that the continuous and relatively stable structures proposed in textbook models of the cytokinetic apparatus need revision. Second, the observation that Ect2 overexpression produces a cell-wide version of what occurs at the equator during cytokinetic apparatus specification suggests that cytokinetic signalling by the spindle might simply reflect redistribution of Ect2 from non-equatorial regions to the equator. More complex scenarios, in which astral microtubules stimulate Rho GAPs in non-equatorial regions or otherwise inhibit Rho, may not be necessary. □

METHODS

Methods and any associated references are available in the online version of the paper.

Note: Supplementary Information is available in the online version of the paper

ACKNOWLEDGEMENTS

Many thanks to S. Maslakova for laboratory space and to B. Dlouhy-Massengale and S. Yang for technical assistance. This work was supported by the National Institutes of Health (GM52932 to W.M.B.) and the National Science Foundation (NSF MCB-0917887 and MCB-1041200 to G.v.D.) and by NIH instrumentation grant 1S10RR026729-01 (K. Eliceiri PI).

AUTHOR CONTRIBUTIONS

W.M.B. and A.L.M. performed frog experiments; G.v.D. and W.M.B. performed starfish experiments. A.B.G. and M.L. developed the model, performed simulations, and conducted data analyses. A.M.M., A.M.K., M.E.L., A.E.G., C.P. and K.-C.S. generated and tested reagents. W.M.B., G.v.D. and A.B.G. wrote the manuscript.

COMPETING FINANCIAL INTERESTS

The authors declare no competing financial interests.

Published online at http://dx.doi.org/10.1038/ncb3251
Reprints and permissions information is available online at www.nature.com/reprints

1. Bement, W. M., Miller, A. L. & von Dassow, G. Rho GTPase activity zones and transient contractile arrays. *Bioessays* **28,** 983–993 (2006).
2. Su, K.-C., Bement, W. M., Petronczki, M. & von Dassow, G. An astral simulacrum of the central spindle accounts for normal, spindle-less, and anucleate cytokinesis in echinoderm embryos. *Mol. Biol. Cell* **25,** 4049–4062 (2014).
3. Green, R. A., Paluch, E. & Oegema, K. Cytokinesis in animal cells. *Annu. Rev. Cell Dev. Biol.* **28,** 29–58 (2012).
4. Rappaport, R. *Cytokinesis in Animal Cells* (Cambridge Univ. Press, 1996).
5. Shuster, C. B. & Burgess, D. R. Transitions regulating the timing of cytokinesis in embryonic cells. *Curr. Biol.* **12,** 854–858 (2002).
6. Canman, J. C., Hoffman, D. B. & Salmon, E. D. The role of pre- and post-anaphase microtubules in the cytokinesis phase of the cell cycle. *Curr. Biol.* **10,** 611–614 (2000).
7. Miller, A. L. & Bement, W. M. Regulation of cytokinesis by Rho GTPase flux. *Nat. Cell Biol.* **11,** 71–77 (2009).
8. Weiner, O. D., Marganski, W. A., Wu, L. F., Altschuler, S. J. & Kirschner, M. W. An actin-based wave generator organizes cell motility. *PLoS Biol.* **5,** e221 (2007).
9. Burkel, B. M., von Dassow, G. & Bement, W. M. Versatile fluorescent probes for actin filaments based on the actin-binding domain of utrophin. *Cell Motil. Cytoskeleton* **64,** 822–832 (2007).
10. Riedl, J. *et al.* Lifeact: a versatile marker to visualize F-actin. *Nat. Methods* **5,** 605–607 (2008).
11. Yoo, S. K. *et al.* Differential regulation of protrusion and polarity by PI3K during neutrophil motility in live zebrafish. *Dev. Cell* **18,** 226–236 (2010).
12. Straight, A. F. *et al.* Dissecting temporal and spatial control of cytokinesis with a myosin II inhibitor. *Science* **299,** 1743–1747 (2003).
13. Su, K.-C., Takaki, T. & Petronczki, M. Targeting of the RhoGEF Ect2 to the equatorial membrane controls cleavage furrow formation during cytokinesis. *Dev. Cell* **21,** 1104–1115 (2011).
14. Benink, H. A. & Bement, W. M. Concentric zones of active RhoA and Cdc42 around single cell wounds. *J. Cell Biol.* **168,** 429–439 (2005).
15. Piekny, A. J. & Maddox, A. S. The myriad roles of Anillin during cytokinesis. *Semin. Cell Dev. Biol.* **21,** 881–891 (2010).
16. Lechleiter, J., Girard, S., Peralta, E. & Clapham, D. Spiral calcium wave propagation and annihilation in Xenopus laevis oocytes. *Science* **252,** 123–126 (1991).
17. Shibata, T., Nishikawa, M., Matsuoka, S. & Ueda, M. Modeling the self-organized phosphatidylinositol lipid signaling system in chemotactic cells using quantitative image analysis. *J. Cell Sci.* **125,** 5138–5150 (2012).
18. Arai, Y. *et al.* Self-organization of the phosphatidylinositol lipids signaling system for random cell migration. *Proc. Natl Acad. Sci. USA* **107,** 12399–12404 (2010).
19. Allard, J. & Mogilner, A. Traveling waves in actin dynamics and cell motility. *Curr. Opin. Cell Biol.* **25,** 107–115 (2013).
20. Goryachev, A. B. & Pokhilko, A. V. Dynamics of Cdc42 network embodies a Turing-type mechanism of yeast cell polarity. *FEBS Lett.* **582,** 1437–1443 (2008).
21. Taniguchi, D. *et al.* Phase geometries of two-dimensional excitable waves govern self-organized morphodynamics of amoeboid cells. *Proc. Natl Acad. Sci. USA* **110,** 5016–5021 (2013).
22. Winfree, A. T. Electrical turbulence in three-dimensional heart muscle. *Science* **266,** 1003–1006 (1994).
23. Von Dassow, G., Verbrugghe, K. J., Miller, A. L., Sider, J. R. & Bement, W. M. Action at a distance during cytokinesis. *J. Cell Biol.* **187,** 831–845 (2009).
24. Murray, A. W. & Kirschner, M. W. Cyclin synthesis drives the early embryonic cell cycle. *Nature* **339,** 275–280 (1989).
25. Gray, N., Détivaud, L., Doerig, C. & Meijer, L. ATP-site directed inhibitors of cyclin-dependent kinases. *Curr. Med. Chem.* **6,** 859–875 (1999).
26. Bement, W. M., Benink, H. A. & von Dassow, G. A microtubule-dependent zone of active RhoA during cleavage plane specification. *J. Cell Biol.* **170,** 91–101 (2005).
27. Rappaport, R. & Ebstein, R. P. Duration of stimulus and latent periods preceeding furrow formation in sand dollar eggs. *J. Exp. Zool.* **158,** 373–382 (1965).
28. Rankin, S. & Kirschner, M. W. The surface contraction waves of Xenopus eggs reflect the metachronous cell-cycle state of the cytoplasm. *Curr. Biol.* **7,** 451–454 (1997).

29. Lim, D. *et al.* The M-phase-promoting factor modulates the sensitivity of the Ca^{2+} stores to inositol 1,4,5-trisphosphate via the actin cytoskeleton. *J. Biol. Chem.* **278,** 42505–42514 (2003).
30. Chang, J. B. & Ferrell, J. E. Mitotic trigger waves and the spatial coordination of the Xenopus cell cycle. *Nature* **500,** 603–607 (2013).
31. Pérez-Mongiovi, D., Chang, P. & Houliston, E. A propagated wave of MPF activation accompanies surface contraction waves at first mitosis in Xenopus. *J. Cell Sci.* **111,** 385–393 (1998).
32. Burkel, B. M., Benink, H. A., Vaughan, E. M., von Dassow, G. & Bement, W. M. A Rho GTPase signal treadmill backs a contractile array. *Dev. Cell* **23,** 384–396 (2012).
33. Charras, G. T., Hu, C.-K., Coughlin, M. & Mitchison, T. J. Reassembly of contractile actin cortex in cell blebs. *J. Cell Biol.* **175,** 477–490 (2006).
34. Berndt, J. D., Clay, M. R., Langenberg, T. & Halloran, M. C. Rho-kinase and myosin II affect dynamic neural crest cell behaviors during epithelial to mesenchymal transition *in vivo*. *Dev. Biol.* **324,** 236–244 (2008).
35. Clay, M. R. & Halloran, M. C. Rho activation is apically restricted by Arhgap1 in neural crest cells and drives epithelial-to-mesenchymal transition. *Development* **140,** 3198–3209 (2013).
36. Holmes, W. R., Carlsson, A. E. & Edelstein-Keshet, L. Regimes of wave type patterning driven by refractory actin feedback: transition from static polarization to dynamic wave behaviour. *Phys. Biol.* **9,** 046005 (2012).
37. Ryan, G. L., Petroccia, H. M., Watanabe, N. & Vavylonis, D. Excitable actin dynamics in lamellipodial protrusion and retraction. *Biophys. J.* **102,** 1493–1502 (2012).

DOI: 10.1038/ncb3251

METHODS

***Xenopus* oocytes and artificially activated eggs.** Chunks of ovaries were removed from anaesthetized, adult female *Xenopus laevis*, rinsed in 1× Barths solution (87.4 mM NaCl, 1 mM KCl, 2.4 mM $NaHCO_3$, 0.82 mM $MgSO_4$, 0.6 mM $NaNO_3$, 0.7 mM $CaCl_2$ and 10 mM HEPES at pH 7.4), and then collagenase treated for 1 h at 17 °C. After extensive rinsing in 1× Barths, oocytes were allowed to recover overnight at 17 °C. After recovery, oocytes were injected with 40 nl of mRNA (0.01–1 mg ml^{-1} needle concentration). Oocytes destined to be imaged as full grown oocytes were maintained at 17 °C overnight and imaged the next day. Oocytes destined to be converted to activated eggs were maintained at room temperature for 3–6 h, then treated with 5 μg ml^{-1} progesterone for 15 min and transferred to 17 °C overnight. The following day, meiotically mature eggs were activated with 10 μg ml^{-1} ionomycin in 0.1× MMR for 2–4 min. Activated eggs (identified by pigment contraction) were rinsed three times in 1× Barths and then maintained at 17 °C for 2 h before imaging. In experiments involving Ect2 overexpression, eggs were subject to a second round of microinjection at 30 min post activation with 10 nl of 0.01 mg ml^{-1} Ect2 mRNA (needle concentration).

***Xenopus* embryos.** Ovulation was induced by injecting adult female *Xenopus laevis* with 600–800 U HCG followed by overnight maintenance at 18 °C. The next day, egg release was promoted by gentle squeezing of the abdomen. Eggs were maintained in 1× MMR (100 mM NaCl, 2 mM KCl, 2 mM $CaCl_2$, 1 mM $MgCl_2$, 5 mM Hepes, pH 7.4), fertilized and then dejellied in 2% cysteine in 0.1× MMR. At the two-cell stage, embryos were microinjected with 5 nl of mRNA at 0.01–1 mg ml^{-1} (needle concentration) or, for the protein version of GFP–rGBD, 5 nl of protein at 1 mg ml^{-1} (needle concentration). In some experiments, a second round of injections took place at the four-cell stage; such injections used a volume of 2.5 nl. Embryos were maintained at 17 °C until imaging.

Starfish. *Patiria miniata* was purchased from Marinus Scientific of Long Beach, California and kept in flowing natural sea water at OIMB. Fragments of gonad were obtained by penetrating the body wall of one arm with a 4 mm biopsy punch. Ovaries were rinsed in calcium-free artificial sea water (CFSW; Stricker and Schroeder's recipe), then teased apart with forceps and shaken gently to release full-size oocytes. We used only oocytes from batches in which most large oocytes were full sized, and in which the spontaneous maturation rate after an hour in CFSW was less than ~25%. Several rinses in CFSW over the course of 1–2 h was sufficient to fully defolliculate oocytes, which were then transferred to 0.22-μm filtered natural sea water (MFSW) before injection. Testis fragments were kept dry in microfuge tubes until needed, and then sperm were obtained by perforating a swollen lobe in MFSW.

Starfish egg handling. While sitting in a dish of sea water, starfish oocytes tend to release mucus that makes handling difficult. Therefore, just before injection, defolliculated oocytes were passed repeatedly through a mouth pipette cut to a diameter slightly exceeding the outer diameter of the oocytes plus jelly coat, ~250 μm. For injection, oocytes were arranged by mouth pipette in rows on coverslip-bottomed dishes (MatTek) that had been coated by washing 30 s with 1% protamine sulphate in distilled water, followed by rinsing in water and air drying. Following injection, oocytes were incubated in MFSW in their injection dishes or transferred to uncoated 35 mm Petri dishes, often with the addition of 50 μg ml^{-1} streptomycin, and kept either at seatable temperature (12–16 °C) or on a Peltier cold plate (Torrey Pines Scientific) at 12–16 °C.

Maturation was induced by addition of 1 mM 1-methyladenine in water to a final concentration of 10^{-6}–10^{-5}. After germinal vesicle breakdown, which usually takes 45–60 min at the temperatures used, maturing oocytes were inseminated by aspirating a suspension of motile sperm from the vicinity of a just-poked testis fragment. Sperm activity, oocyte binding, and fertilization success (as judged by envelope elevation) were observed carefully under a dissecting microscope, because of the high risk of polyspermy in microinjected oocytes.

For some experiments, fertilized eggs were deprived of their envelope by brief treatment with 1% sodium thioglycolate in MFSW at pH 9.5–10.0 followed by several transfers to normal MFSW. Thioglycolate solution was made fresh within an hour or two of use, and titrated by addition of 1 M KOH while stirring vigorously. During and after envelope dissolution, eggs were kept well separated in agarose-coated 35 mm Petri dishes. Gentle shearing with a mouth pipette during treatment speeds removal of coats (that is, before full dissolution), limiting the time spent in high-pH seawater.

Microinjection and micromanipulation. For *Xenopus*, pressure microinjections were performed with a PLI-100 picoinjector (Medical Systems Corp.) using needles pulled from capillary tubes and calibrated using oil and a stage micrometer. Oocytes were microinjected in 1× Barths in a 5 ml Petri dish with plastic mesh affixed to the bottom; embryos were microinjected in 0.1× MMR + 5% Ficoll in a meshed dish.

Starfish oocytes were injected in coverslip-bottomed dishes on an inverted microscope at 18–20 °C using an oil-hydraulic manipulator (Narishige), pressure injector (Dagan), and glass needles pulled from 1 mm OD filament-containing capillaries (Sutter) using a P-97 Flaming-Brown puller (Sutter). Before loading, pulled needles were silanized by adding ~100 μl hexamethyldisilazane to a closed box containing the needles. Backfilled needles were broken to appropriate size (3–5 μm) against a coverslip fragment held to the bottom of the injection dish with high-vacuum grease. In our hands, starfish oocytes tend to eject the germinal vesicle if the needle penetrates it; therefore, we systematically injected into the cytoplasm a puff corresponding to <1% of oocyte volume.

To generate anucleate cytoplasts or locally apply drugs, fertilized eggs were stripped of their fertilization envelopes and then arranged in coverslip-bottom dishes. Bisections were performed with an injection needle held by an oil-hydaulic micromanipulator. Local drug applications were conducted by filling a large-bore (20–50 μm), fire-polished drawn capillary with 0.5% low-melt agarose containing latrunculin B at 0.5–5 μM. Roscovitine and nocodazole treatment do not require envelope removal, and global, timed drug application was accomplished by trapping small groups of oocytes between a slide and coverslip, and then flooding one open chamber edge with drug-containing MFSW while wicking away medium from the opposite opening with filter paper.

Actin staining. *Xenopus* embryos were rinsed 3× in PBS (phosphate-buffered saline—100 mM NaCl, 3 mM KCl, 10 mM Na_2HPO_4, 2 mM KH_2PO_4, pH 7.4) and fixed for 1 h at room temperature in Zevon's fixative (100 mM KCl, 10 mM Hepes, 3 mM $MgCl_2$, 1 mM EGTA, pH 7.6) +3.7% fresh paraformaldehyde, 0.1% glutaraldehyde, 0.1% Triton X-100, and 1 U ml^{-1} AX-488 phalloidin (Molecular Probes). Embryos were then washed 3× 10 min in PBS, and then 1 h in TBSN (Tris-buffered saline—50 mM Tris, pH 7.5, 150 mM NaCl + 0.1% NP-40).

Imaging. Frog oocytes, activated eggs, and embryos were imaged using a Prairie View Laser Scanning Confocal (Bruker Nano Surfaces) on a Nikon Eclipse Ti. Samples were prepared as described previously[38] and imaged using a 40× 1.0 NA or a 60× 1.4 NA objective.

All imaging of starfish oocytes and embryos was conducted on an Olympus FluoView 1000 laser-scanning confocal on an IX81 inverted stand, using 60 × 1.2 NA or 40 × 1.15 NA water-immersion objectives, or a 20× dry 0.75 NA objective. Cells were either held between a slide and coverslip separated by two ridges of high-vacuum grease (Dow Corning) and compressed to trap the cells, or were filmed in ethanol-cleaned coverslip-bottomed dishes; clean glass clings just enough to demembranated oocytes that they are prevented from drifting off, but not rendered overtly abnormal. To keep cells at viable temperatures, we used stage-mounted Peltier cooling adaptors (Dagan) set to 12–14 °C. When using coverslip-bottomed dished filled with sea water and water-immersion objectives, in-bath measurements and comparison of developmental rates with controls suggest an effective temperature 1–3 °C above the set point, slightly more for cells held in slide chambers. Volumes of sea water and numbers of oocytes per dish or slide were limited to avoid anoxia (10–20 embryos per slide preparation; <50 in dishes).

Constructs and *in vitro* synthesis of mRNA. The following constructs used were described previously and for both frog and starfish injected at concentration ranges as follows: eGFP–rGBD (ref. 14), 100–500 ng μl^{-1}; mCh–UtrCH (ref. 9), 100–200 ng μl^{-1}; mCh–H2B, 50 ng μl^{-1}; 2×mCh EMTB, 50–200 ng μl^{-1} (ref. 23); 1×GFP, 3×GFP– or 3×mCh–SpEct2 (ref. 2), 10–50 ng μl^{-1}; anillin–3×GFP, 100 ng μl^{-1} (ref. 39). 3×GFP–rGBD was generated by cloning rGBD into pCS2+ downstream of 3 tandemly repeated GFPs and was injected at 800 ng nl^{-1}. *Xenopus* Ect2 (Open Biosystems) was cloned into pCS2+ and dominant negative *Xenopus* Ect2 was made by changing the conserved residues 593PVQR596 in the catalytic domain to alanines[2,13] using a Quikchange kit (New England Biolabs) and the following primers: F:5′—cttatcagagctgctgcagcattaccaagcgtcgctcttcttctg-3′; R:5′-gcgacgcttggtaatgctgcagcagctctgataagtaactcgac-3′. Wild-type *Xenopus* Ect2 was injected at 5–10 ng μl^{-1}; dominant negative *Xenopus* Ect2 was injected at 50–100 ng nl^{-1}. Δ90 cyclin was made by cloning full-length human cyclin B into pCS2 and then removing the first 270 nucleotides; it was injected at 50 ng μl^{-1} for both frog and starfish. mRNAs were transcribed from linearized plasmids *in vitro* using the mMessage mMachine SP6 kit (Ambion) and were polyadenylated using a Poly(A) tailing kit (Ambion).

Expression of FLAG–GFP–rGBD. A 5′ terminal Kozak consensus sequence and FLAG epitope were added to the GFP–rGBD construct from ref. 14 using PCR. The resultant amplicon was inserted into the bacmid donor plasmid pFastBac1 to generate recombinant bacmid DNA in DH10Bac (Invitrogen) bacteria. Recombinant baculovirus was produced in Sf21 insect cells and used to infect additional Sf21 monolayers. Recombinant protein was purified using anti-FLAG M2 affinity resin (Sigma) with Arg-based elution[40]. Elution fractions were pooled and the protein concentrated to 50 μM in 25 mM HEPES, 100 mM KCl pH 7.5 before oocyte injections.

Image processing. All image processing (projection, brightness and contrast, averaging, and so on) was conducted in ImageJ, except for false colouring and figure composition in Photoshop CS6. All kymographs were prepared in ImageJ by re-slicing a strip of a time series (as shown by outlines in figures), 6 or 12 pixels wide (~1 μm), then averaging the re-slicing planes and stretching along the time axis for clarity, with or without bicubic interpolation. Subtraction was performed in ImageJ using the image calculator function, and then median filtered (3 × 3) to reduce noise. No other convolution filters or other image processing was applied to any image. For greyscale images, adjustments were limited to white and black points, preserving the linearity intensity range between. For certain data, pseudocolour tables were used to perceptually balance bright versus dim features while preserving luminosity in single-channel images (the Abattoir Blues lookup table in Figs 3c,d, 7a,b,e, and 8h) or to blend two channels while providing a distinct colour for co-localization (the Copper/Malachite lookup table in Figs 4a–e, 5g,h and 8a–g, and Supplementary Fig. 5). Colour tables for both are reproduced adjacent to several figure panels that make use of the range. Identical colour tables were used for supplementary videos, but with gamma adjustment to un-do a non-user-controlled gamma adjustment applied by the QuickTime H.264 codec.

Data analyses. For most analyses, the data were extracted with ImageJ from experimental time-lapse videos of Rho and F-actin dynamics in the form of kymographs, that is, matrices u^{R}_{ij}, u^{A}_{ij}, where index i represents time and index j is the spatial position of an image pixel along a chosen linear segment. Spatial and time correlation analyses were performed according to the standard signal processing method; for example, the time autocorrelation function for the Rho signal at a specific pixel j is given by

$$C^{R}_{j}(\tau) = \int_{0}^{t} u^{R}_{j}(t+\tau)u^{R}_{j}(t)\mathrm{d}t$$

where the integral is taken along the jth column of the data kymograph. To obtain statistical information (Fig. 4f,g), computed spatial and time correlation functions were averaged over multiple lines and columns of the kymograph, respectively. Furthermore, for the computation of the spatial autocorrelation function, kymographs were taken over multiple varied spatial directions on the images.

To compute the statistical distribution of wave runs, the above kymographs were first normalized to lie within [0,1] and then processed using the MATLAB function contourf() that performs non-polynomial interpolation and contour extraction in two-dimensional images. The candidate positions of the wavefront were then extracted at locations of the contour computed at the half-maximal height, 0.5. At each contour point its slope was computed with a centred 5-point template. To separate waves from non-propagating excitable dynamics, only points with a slope above a suitable threshold calculated on the basis of spatial and temporal resolution of the original time-lapse video were retained for the following analysis. All candidate runs shorter than 4 consecutive time points (frames) were discarded from the analysis. The lengths of these unbroken wave runs were then binned and used for the calculation of a histogram representing the statistical distribution of wave runs.

For the kinetic analysis[17] (Fig. 5a–c and Supplementary Fig. 4a–c), in addition to signal values, time derivatives d[Rho]/dt and d[actin]/dt were calculated numerically from the kymographs using finite-difference approximation. The data were then suitably binned and the average and standard deviation were computed per bin to reveal the dependences between the Rho and F-actin signals. To reconstruct the phase of the excitable dynamics, we implemented Morlet wavelet analysis[21] using MATLAB. For the time series of Rho or F-actin signal at a given image pixel, this method generates two two-dimensional functions, amplitude and phase (Supplementary Fig. 4d). The maximal value of amplitude for each given time point defines the dominant value of the time period $T(t)$, which need not be the same for all time points. Morlet wavelet analysis, thus, allows one to determine the phase even when the periodicity of the signal changes with time. In the case shown in Supplementary Fig. 5d, $T = 80$ s uniformly within the time series. The curve of amplitude maxima (in this case, a straight line segment) is then transferred onto the Morlet phase function and the value of the phase at each time t is read along the curve. The value of the phase ($-\pi$:π) is then computed in each image pixel and time point and plotted as a colour-coded value (Fig. 5d–f). This method reveals spiral wave cores that are seen as the spatial points in which all rainbow colours come together even in very noisy data, where interaction of multiple unstable spiral waves makes it impossible to directly observe contiguous spirals by eye.

The change in the wave pattern of the cortical dynamics observed throughout the cell cycle prompted us to introduce the activity ratio, a heuristic measure of the fraction of the full period that the system spends in the excited state. To compute the activity ratio in space (Supplementary Fig. 6b,c), the average value of the normalized signal of Rho or F-actin is computed first along the ith line of the data kymograph. The data are then converted to 1 if the pixel value is above the average and to 0 if below. Activity ratios are then computed as shown in Supplementary Fig. 6b for every spatial period and averaged along the ith line of the kymograph. This value is the activity ratio at time t (Supplementary Fig. 6c). Larger statistics was obtained by averaging over multiple kymographs. As shown in Supplementary Fig. 6, the thus defined activity ratio is easily computed even from noisy experimental data and can be readily compared with the behaviour of the model (see below).

Modelling. The model (Fig. 8a,b) consists of three reaction–diffusion equations representing dynamics of active (RT) and inactive (RD) Rho (ref. 20) as well as the density of polymeric F-actin (F) that does not diffuse. Diffusion of RT and RD is explicitly represented by the diffusion terms $D_{RT}\Delta RT, D_{RD}\Delta RD$, where Δ is the Laplace operator. The numbers on the reaction arrows in Fig. 8a (shown in curly braces {} below) correspond to the numbers of the reaction rate constants in Fig. 8b (values given in Supplementary Fig. 6a). In our model, we explicitly consider only the dynamics of membrane-bound active and inactive forms of Rho and assume that the inactive form, RD, is freely exchanging with a constant large pool in the cytoplasm ({5} k_5, {6} $-k_6 RD$). Reaction term R describes nucleotide cycling of Rho and includes activation of Rho potentially by several GEFs ({0} $k_0 RD$) of which GEF activity of Ect2 is singled out explicitly ({1, 2, 11} $[\mathrm{Ect2}]RT^2RD/(k_2^2 + RT^2)$, $[\mathrm{Ect2}] = [\mathrm{Ect2}]_0 k_1 \times (1 + k_{11}RT)$) to highlight the autocatalytic character of Rho activation by means of Ect2. Inactivation of Rho is assumed to be both constitutive ({3} $-k_3 RT$) and F-actin-dependent ({4} $-k_4 F \times RT$); the latter term reflects F-actin-mediated negative feedback to the activity of Rho. F-actin polymerization is a weak constitutive process in the absence of Rho activity ({7} k_7) and is significantly stimulated by the active Rho ({8, 9} $k_8 RT^2/(k_9^2 + RT^2)$). Depolymerization of actin, for simplicity, is taken to be an unregulated first-order reaction ({10} $-k_{10}F$). Molecular fluctuations that are necessary for the induction of excitable dynamics are taken into consideration by the stochastic term $\mathrm{d}W(\sigma, s)$ that denotes spatially distributed Gaussian white noise with mean 0, standard deviation σ and spatial correlation length s. Unknown membrane diffusion coefficients of active and inactive Rho, D_{RT}, D_{RD}, were varied in the ranges shown (Supplementary Fig. 6a). Other model parameters were chosen to fit the dynamics observed experimentally in starfish cells. In particular, the model reproduces the characteristic wavelength and the temporal period of excitable dynamics as well as the time delay between the Rho and F-actin maxima.

To model wave dynamics observed in starfish oocytes between consecutive M-phases (Fig. 8c–e and Supplementary Fig. 6c), it was assumed that temporal activity of Ect2 is governed by a Gaussian function $TG(t) = [\mathrm{Ect2}]_0(1 + \exp(-(t - t_0)^2/2\tau^2))$, where t_0 and $\tau = 80$ s were estimated from the imaging data. To simulate furrow formation in mitotic starfish cells (Fig. 8f,f′), Ect2 temporary activity given by $TG(t)$ was assumed to be further modulated by a spatially dependent term $SG(x,t) = \exp(-(x - x_0)^2/2\beta(t)^2)$, where x is the spatial dimension that spans the pole-to-pole distance L of a mitotic cell and $\beta(t)$ decreases linearly in time from L to $l_f = 7$ μm, the furrow width estimated from the data. To simulate depolymerization of microtubules by nocodazole (Fig. 8g,g′), the Ect2 concentration profile was rapidly relaxed to a spatially uniform distribution with an equivalent total quantity of Ect2. Model reaction–diffusion equations were solved with the standard forward Euler finite-difference method using a custom-developed C code.

All computer codes generated in this study are freely available from the authors on request.

Reproducibility of experiments. All of the results reported were replicated at least three times to ensure repeatability; the basic results—for example, Ect2-amplifiable actin and Rho waves—were replicated 60 or more times. The only issues with reproducibility arose when probes were under- or over-expressed or when too much Ect2 was expressed (this resulted in contractions that were either too extreme to film or that resulted in cell lysis). The specific number of repeats is indicated in each figure legend.

38. Woolner, S., Miller, A. L. & Bement, W. M. Imaging the cytoskeleton in live Xenopus laevis embryos. *Methods Mol. Biol.* **586,** 23–39 (2009).
39. Reyes, C. C. *et al.* Anillin regulates cell-cell junction integrity by organizing junctional accumulation of Rho-GTP and actomyosin. *Curr. Biol.* **24,** 1263–1270 (2014).
40. Futatsumori-Sugai, M. *et al.* Utilization of Arg-elution method for FLAG-tag based chromatography. *Protein Expr. Purif.* **67,** 148–155 (2009).

nature cell biology

DOI: 10.1038/ncb3251

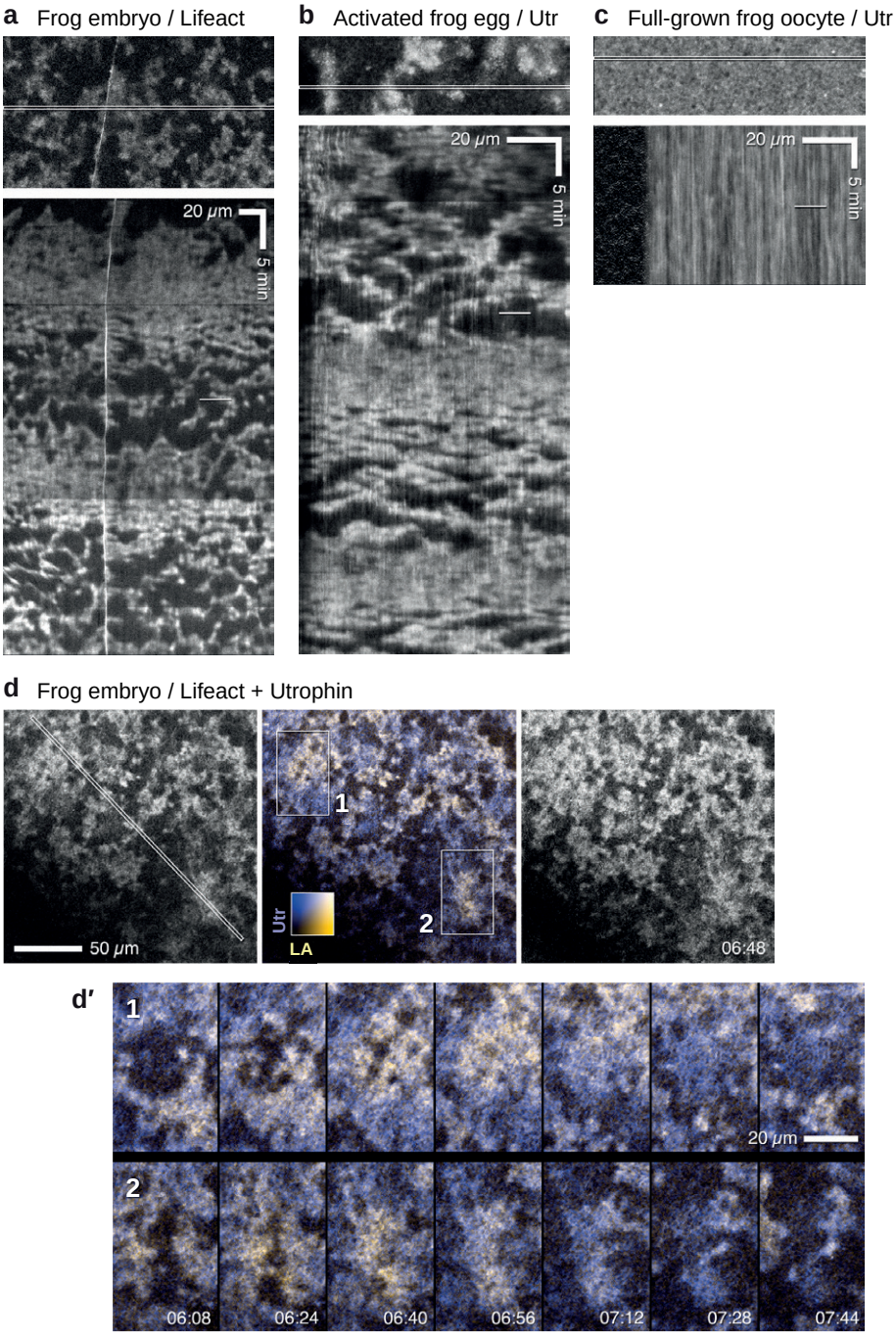

Supplementary Figure 1 Cortical waves of actin assembly and disassembly in activated frog eggs and embryos. (**a**) Surface view of frog blastomeres expressing GFP-lifeact to label F-actin. Top: single frame; cortical F-actin consists of irregularly sized patches throughout cortex, which, as illustrated in the kymograph made from the outlined region (bottom) travel continually across the surface. Bottom: In the kymograph, F-actin waves create slanted bands with semi-regular spacing. (b) High magnification surface view of activated frog egg expressing GFP-UtrCH. Top: single frame; cortical F-actin consists of irregularly sized patches, which, as illustrated in the kymograph made from the outlined region (bottom) travel continually across the surface. Bottom: In the kymograph, F-actin waves create slanted bands with semi-regular spacing. (c) High magnification surface view of full-grown (prophase 1-arrest) frog oocyte expressing GFP-UtrCH. Top: single frame; cortical F-actin is relatively uniform with no obvious patches and no apparent waving behavior as illustrated in the kymograph made from the outlined region (bottom). Bottom: In the kymograph, cortical F-actin is quite stable. (d) Single frame from time-series of frog embryo co-expressing GFP-Lifeact and mCherry-UtrCH, single channels with pseudocoloring as shown in swatch (pure Lifeact would be yellow; pure UtrCH would be blue; equal blend of each by intensity would be gray). Diagonal band on left panel is the zone for kymograph in Fig. 1d; boxed regions 1 and 2 blown up 2x in d' show wave fronts colliding. In each, the wave fronts are initially yellowish, turn bluish after collision, then fade. Images are representative of at least 10 (a), at least 30 (b) or 3 (c, d)independent experiments, respectively.

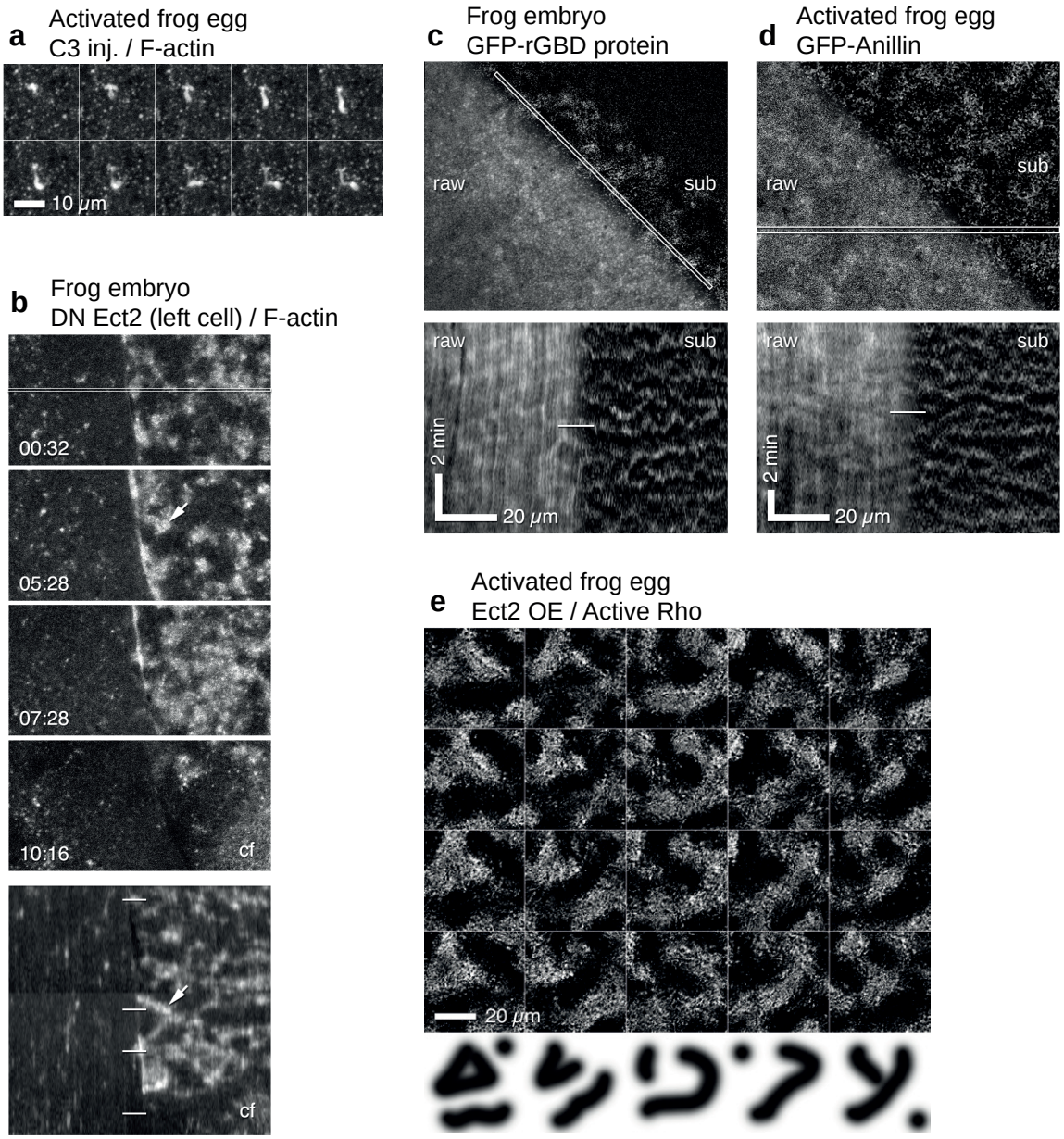

Supplementary Figure 2 Cortical Rho activity waves and Rho- Ect2-dependence of cortical F-actin waves in activated frog eggs and frog embryos. (**a**) Time-lapse sequence from activated frog egg expressing GFP-UtrCH to label F-actin and injected with C3 exotransferase to inhibit Rho (6 s intervals). No cortical F-actin waves are present but actin assembly occurs nonetheless as shown by comet like movement of F-actin-associated invagination. (**b**) Frog embryo expressing GFP-UtrCH and then microinjected with dominant negative Ect2 (left blastomere) or, as a control, nothing (right blastomere); top-still frames, bottom, kymograph. Dominant negative Ect2 eliminates the F-actin waves in the dominant negative Ect2 expressing cell. (**c**) Frog embryo microinjected with recombinant GFP-rGBD protein to label active Rho. Single frame (top) and kymograph (bottom), raw (left) and subtracted data (right, t_0–t_{-3}), highlighting rising Rho activity. The kymograph demonstrates that what otherwise looks like mundane inhomogeneity in the still image actually reflects regular waves of Rho activity; these are more evident in the processed half of both the image and kymograph. (**d**) Activated frog egg expressing GFP-anillin. Single frame (top) and kymograph (bottom), raw (left) and subtracted data (right, t_0–t_{-3}), highlights waves of cortical anillin recruitment. (**e**) Time-lapse sequence from activated frog egg expressing 3XGFP-rGBD to label active Rho and overexpressing Ect2. Top: Each panel is 20 s after previous panel. While the Rho wave patterns change rapidly every 20 s, note the repetition evident every 100 s (compare panels as columns). Bottom: inverted, black and white representation of dominant wave pattern in each column. Images are representative of 3 (a, b, d), 4 (c) and 6(e) independent experiments, respectively.

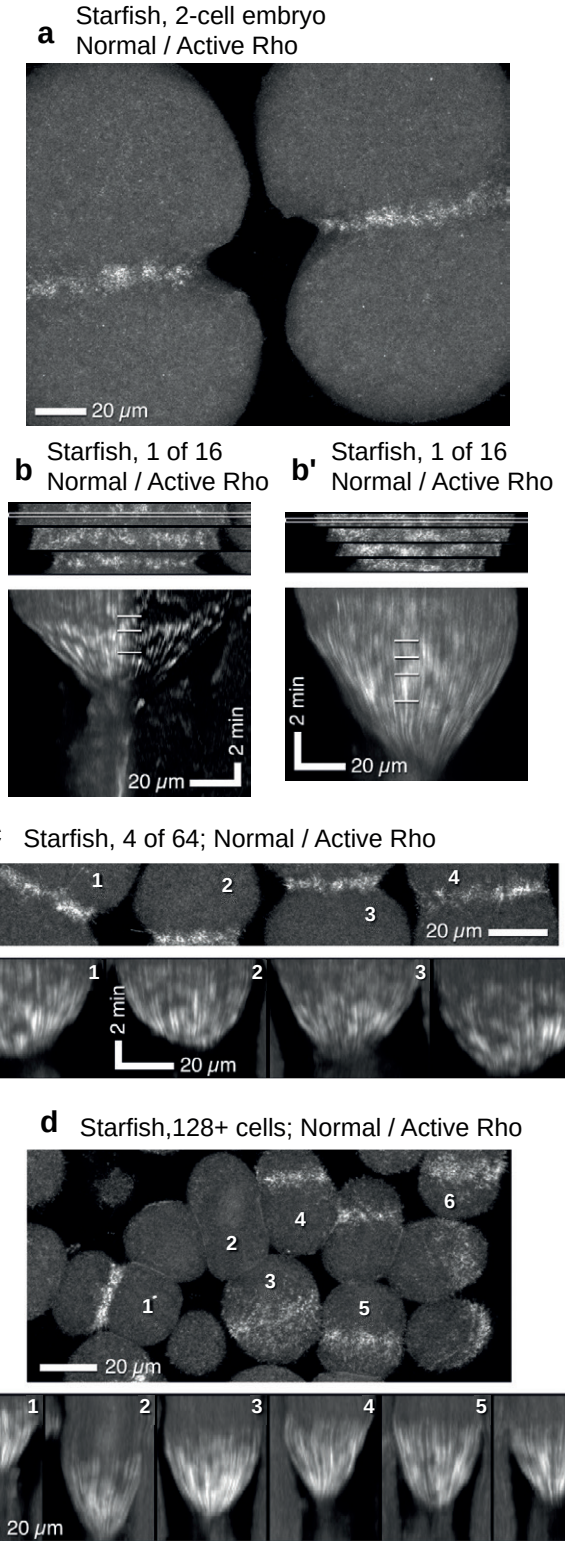

Supplementary Figure 3 Cortical Rho activity waves in starfish blastomeres. (**a**) Image from time-lapse movie showing waves of cortical Rho activity within ingressing zygote furrows. (**b,b'**) Top: Images from time-lapse movie showing cortical Rho activity waves at equator of dividing blastomeres. Bottom: kymographs taken from blastomeres above. Waves persist during much of furrow ingression. See Supplementary Video 22. (**c**) Top: Image from time-lapse movie showing cortical Rho activity at equator of four different blastomeres. Bottom: kymographs taken from blastomeres above. Waves are present during ingression. See Supplementary Video 23. (**d**) Top: Image from time-lapse movie showing cortical Rho activity in later, smaller blastomeres than those in **a-c**. Rho activity at equator is more continuous. Bottom: Kymographs taken from blastomeres indicated above. Rho activity is largely continuous rather than wave-like. See Supplementary Video 24. Images representative of 4 independent experiments.

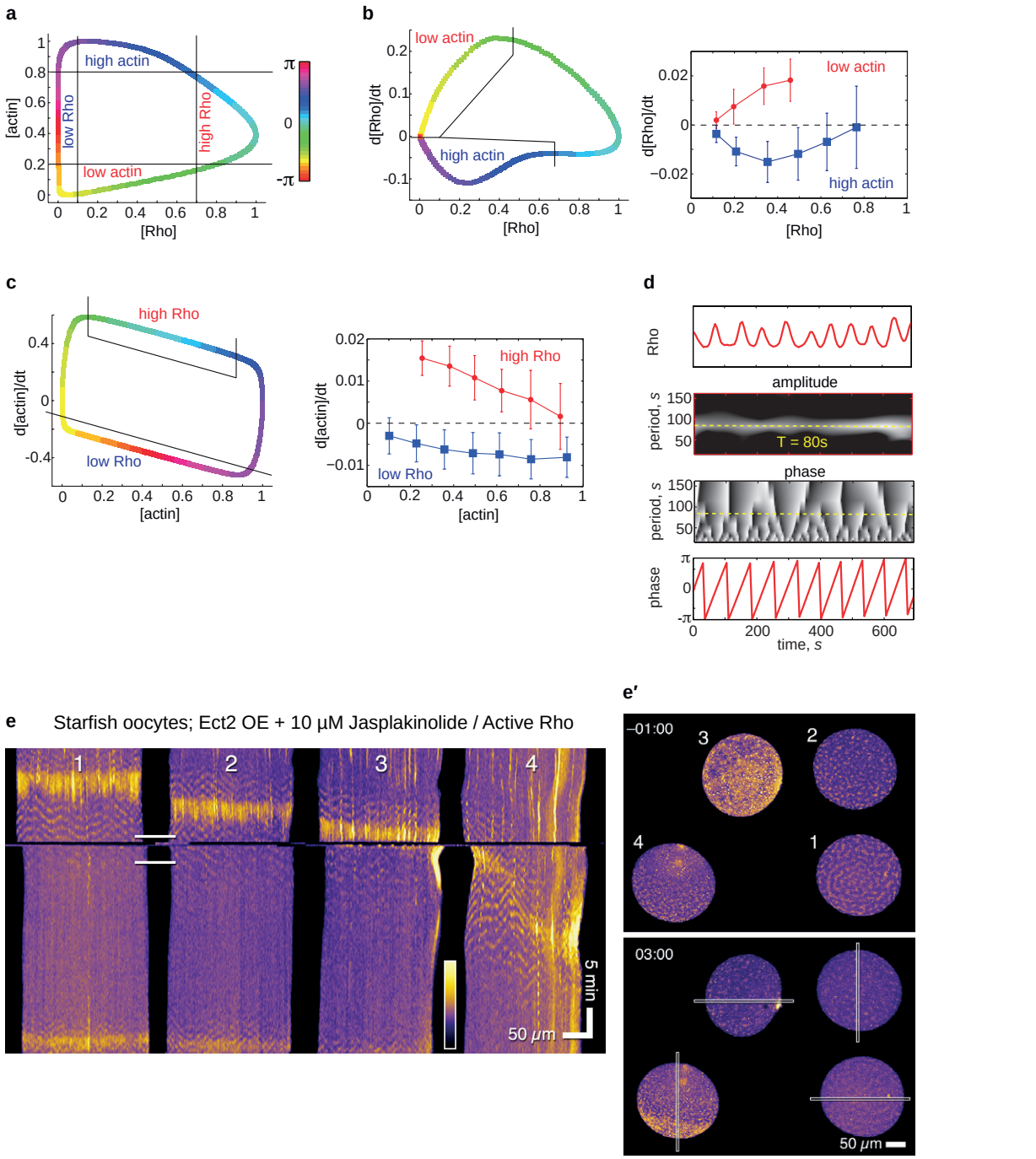

Supplementary Figure 4 Reconstruction of excitable dynamics. (**a**) Projection of full wavelength onto plane of normalized concentrations (Rho, actin) generates a closed loop parameterized by phase (-π,π) and color-coded. Loop computed using activator-inhibitor model introduced here. Domain boundaries of high/low values of Rho and F-actin used to reconstruct kinetic relationships in panels b, c denoted by straight-line segments. (**b**) Left panel: activator-inhibitor model prediction (Rho – activator, F-actin – inhibitor) for dependence of d[Rho]/dt on [Rho] based on panel a. Parameterization by phase shown for comparison with a. Right panel: d[Rho]/dt versus [Rho] from images (see Methods). Data shown as mean ± std. Note qualitative agreement between data and model prediction. (**c**) Left panel: activator-inhibitor model prediction (Rho – activator, F-actin – inhibitor) for dependence of d[actin]/dt on [actin] based on panel a. Right panel: d[actin]/dt versus [actin] from images. Note qualitative agreement between data and model prediction. Results are mean ± SD; n=900 cycles. (**d**) Phase of excitable dynamics reconstructed from Rho time series (top panel) measured at cortex. Morlet transform of time series generates amplitude and phase functions for every time point and candidate temporary period of dynamics. Amplitude maxima (yellow dashed line) show how most likely value of period *T* depends on time (here, *T = 80s*). *T = 80s* line is projected onto the Morlet phase function and a single time-dependent value of phase (bottom panel) is read along that line (yellow dashed line). (**e**) Rho wave attenuation in Ect2-overexpressing starfish oocytes treated with 10 µM Jasplakinolide during first meiosis; kymographs made from strips indicated in e', numbered by order of anaphase entry. Gap in kymographs shows time of drug addition. Jasplakinolide induces slow accumulation of excess cortical actin but does not completely abolish actin turnover (not shown). Before drug addition, oocytes 1-3 exhibited prominent waves; without treatment, waves typically continue about half the time between metaphases I and II; in three of these cells, jasplakinolide rapidly reduces wave amplitude (the fourth may not have experienced the same concentration of drug). e' displays wave patterns just before and shortly after drug addition. Images are representative of 3 independent experiments.

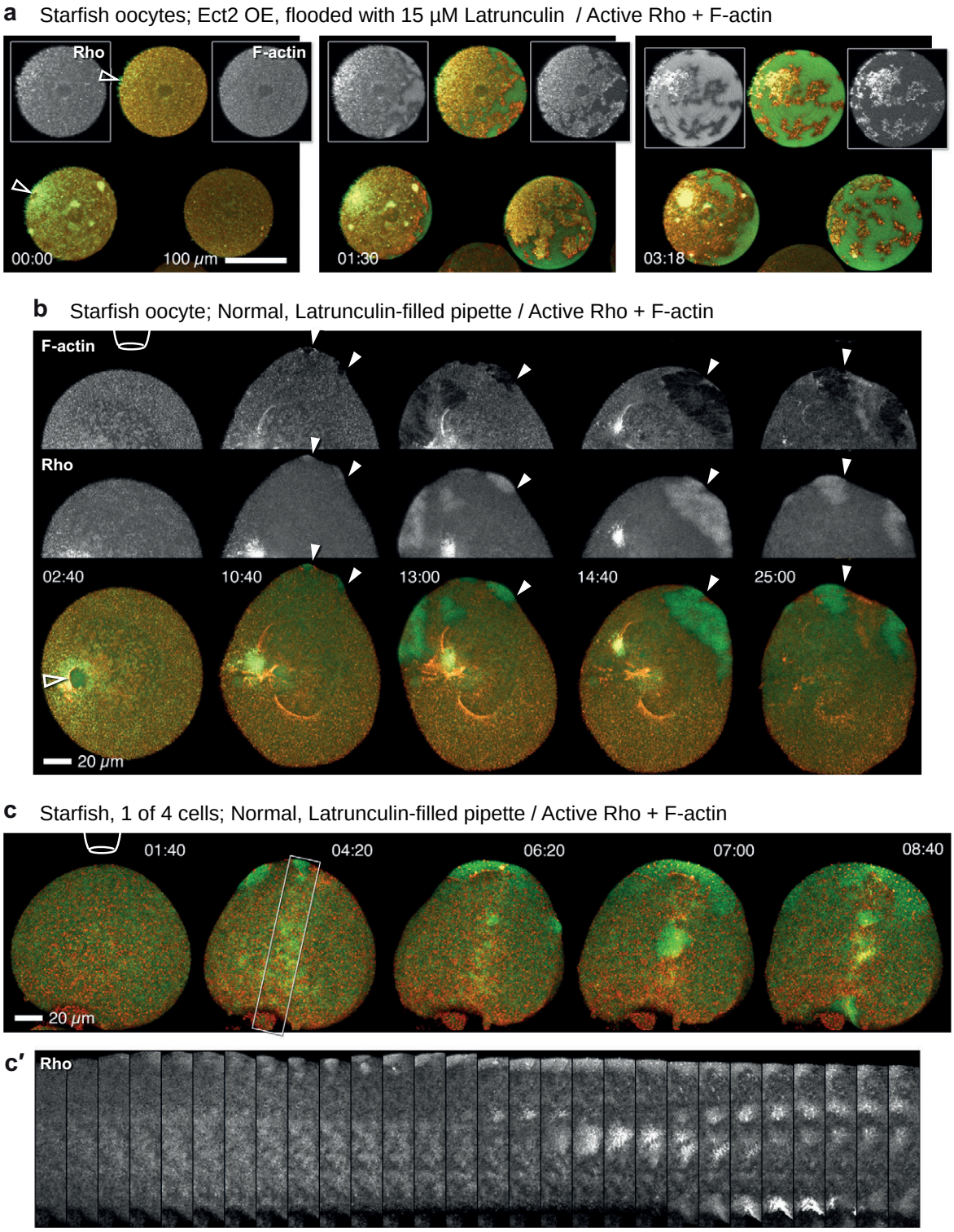

Supplementary Figure 5 Cortical F-actin antagonizes Rho activation. (**a**) Time-lapse series showing active Rho (malachite) and F-actin (copper) in merge or as single channels in starfish oocyte overexpressing Ect2 and subject to global treatment with latrunculin. Shortly after latrunculin application the entire cortical F-actin network shatters, an event accompanied by a transient and global increase of Rho activity. Arrowhead indicates site of meiotic spindle. (**b**) Time-lapse series showing active Rho (malachite) and F-actin (copper) in merge or as single channels in normal (i.e., non-Ect2 overexpressing) starfish oocyte subject to local F-actin disassembly at site indicated by pipet tip schematic. As in cells overexpressing Ect2 (Fig. 5g,h) local F-actin disassembly is accompanied by a burst of Rho activation. Hollow arrowhead indicates site of meiotic spindle; filled arrowheads indicate bursts of Rho activity. (**c**) Time-lapse series showing active Rho (malachite) and F-actin (copper) in normal starfish blastomere subject to local F-actin disassembly at site indicated by pipet tip schematic. Loss of cortical F-actin from the equator (white rectangle) produces a burst of Rho activity just as it does elsewhere on cell cortex. (**c"**) Images of equator taken from time-lapse movie of cell above showing bursts of Rho activation following F-actin disruption within nascent furrow. Images are representative of 6 (a) and 3 (b, c) independent experiments, respectively.

a

k_0	$0.026\ s^{-1}$	k_8	$0.1\ \mu M\, s^{-1}$
k_1	$1.2\ \mu M^{-1} s^{-1}$	k_9	$0.2\ \mu M$
k_{11}	$0.58\ \mu M^{-1}$	k_{10}	$0.03\ s^{-1}$
k_2	$0.8\ \mu M$	D_{RT}	$0.03 \div 0.1\ \mu m^2/s$
k_3	$0.2\ s^{-1}$	D_{RD}	$0.04 \div 1.0\ \mu m^2/s$
k_4	$0.6\ \mu M^{-1} s^{-1}$	σ	10^{-3}
k_5	$4\ \mu M\, s^{-1}$	s	$2\ \mu m$
k_6	$4\ s^{-1}$	$[Ect2]_0$	$1 \div 2\ \mu M$
k_7	$0.02\ \mu M\, s^{-1}$		

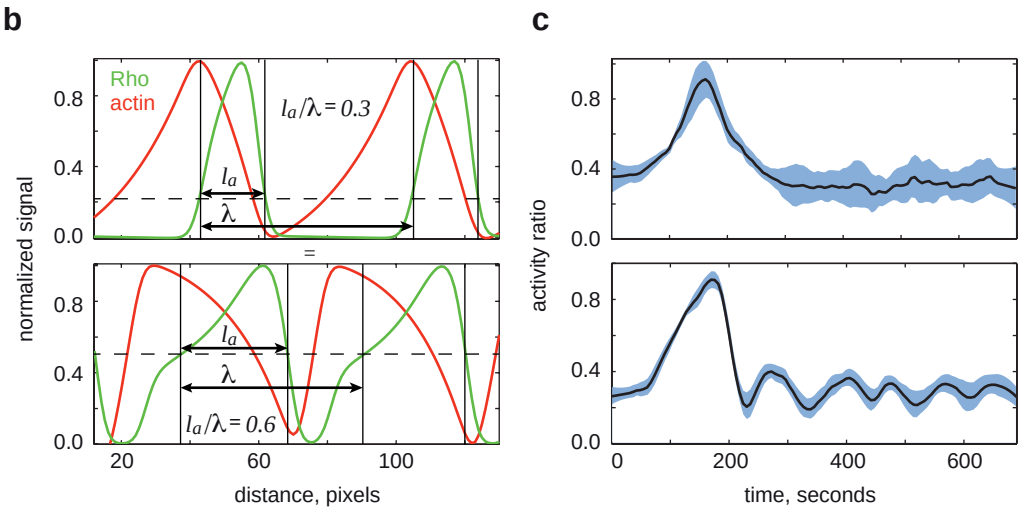

Supplementary Figure 6. Computational model of excitable cortical dynamics. (**a**) A set of parameters used for model simulations has been chosen to fit the temporal period and dominant wavelength of excitable wave pattern as well as the time shift between Rho and F-actin signals observed in starfish oocytes overexpressing Ect2. (**b**) The model predicts that the increase in Ect2 activity results in the change of the wave pattern that can be quantified by the activity ratio, which is defined as l_a/λ, the fraction of the wavelength λ where the value of normalized Rho signal is above 50% of the average over one wave period. Top panel: At the Ect2 activity generating the wave pattern typical of meiotic starfish oocyte interphase ($[Ect2]_0$ = 1 μM), activity ratio is 0.3. Bottom panel: Increase in Ect2 activity ($[Ect2]_0$ = 2 μM) results in the wave pattern with broad wave crests and narrow refractory zones; activity ratio is 0.6. Average level of normalized Rho signal is indicated by dashed line. (**c**) The model predicts that the wave pattern observed in meiotic starfish oocytes during polar body emission can be explained by an increase in Ect2 activity. Top panel: Activity ratio computed from the experimental data (see Methods for details). The peak in activity ratio corresponds to polar body emission. Bottom panel: Activity ratio computed from the results of simulation with changing activity of Ect2. Data are shown as mean ± SD.

Supplementary Videos Legends

Supplementary Video 1. Surface view of cleaving blastomere in mid-cleavage stage frog embryo (one of 32+ cells) expressing GFP-Utr, single optical plane, 2.4 sec/frame at 30 fps (time in seconds). Corresponds to Figure 1a. F-actin foci come and go rapidly, transiently increasing in density to near-uniformity shortly before cytokinetic furrow formation, whereafter the density declines again.

Supplementary Video 2 High-magnification surface view of activated frog egg expressing GFP-Utr, single optical plane, 4 sec/frame at 30 fps (time in min:sec). Corresponds to Figure 1b, without color coding. Kymograph scrolling beneath frame sequence made by averaging across the rectangle indicated. This sequence spans two apparent M-phases in 46 minutes, after each of which F-actin density transiently increases to near uniformity. Between these pulses, waves continually traverse the surface with apparently random direction changes; cable networks are frequently apparent between the margins of fading wave fronts.

Supplementary Video 3 Cleaving frog blastomere expressing both GFP-Utr (blue) and Lifeact-mCherry (yellow); single optical plane, 12 sec/frame at 30 fps (time in min:sec). Corresponds to Figure 1d. Throughout, leading wave fronts are yellowish, whereas trailing edges, and cable networks left in the wake of passing waves, are white or bluish. Note, as shown in Fig. 1d, that GFP-Utr and Lifeact-mCherry both label the same structures – that is, there is no pure color in this sequence, all structures contain some blue and some yellow.

Supplementary Video 4 Surface view of activated frog egg expressing 3xGFP-rGBD, average projection of 4 1 micron sections, 10 sec/frame at 15 fps (time in min:sec). Corresponds to Figure 2c. 20-min. sequence plays twice, the second time alongside a median-filtered rearward subtraction (current time minus three frames previous). This highlights the subtle waves traveling across a background of low-level cortical Rho activity.

Supplementary Video 5 Surface view of activated frog egg expressing 3xGFP-rGBD plus wild-type *Xenopus* Ect2, average projection of 4 1 micron sections, 10 sec/frame at 15 fps (time in min:sec). Corresponds to Figure 2d. 20-min. sequence plays twice, the second time alongside a median-filtered rearward subtraction (current time minus three frames previous). Compared to normal cells (Fig. 2c, Video 4) waves of Rho activity are far more pronounced. Not only is the amplitude greater, waves appear to occur in quasi-repeating patterns, and individual wave fronts continue further across the surface before dissipating or colliding with other waves.

Supplementary Video 6 Medial focal slabs of two starfish oocytes expressing GFP-rGBD, one with extra wild-type *S. purpuratus* Ect2. Both sequences cover first meiosis with polar body emission. First sequence (normal oocyte) is a max. projection of 8 1 micron sections, second sequence (Ect2 over-expressing) is a max. projection of 8 1.5 micron sections; both are 20 sec/frame at 15 fps (time in min:sec). Correspond to Figures 3a and 3b. In the normal oocyte, a broad coherent wave of Rho activity initiates at the vegetal pole, passes toward the animal pole, and "breaks" around the meiotic spindle, coalescing into the cytokinetic zone that pinches off the polar body. With extra Ect2, the single coherent wave breaks up into brighter, more persistent wavelets, which continue throughout and after polar body emission. Second sequence plays twice, the second time with the first sequence inset for comparison.

Supplementary Video 7 Surface view of Rho waves in starfish oocyte expressing GFP-rGBD and wild-type *S. purpuratus* Ect2, max. projection of 11 1 micron sections, 12 sec/frame at 15 fps (time in min:sec). Corresponds to Figure 3c. This sequence covers second meiosis; first polar body has been successfully extruded already. Waves start just before second polar body emission, show a global increase in intensity, then settle into a regime with prominent, well-spaced fronts that travel tens of microns with consistent direction. As highlighted by insets in Fig. 3c, approximately repeating patterns emerge post-meiotically.

Supplementary Video 8 High-magnification surface view of Rho waves in normal starfish oocyte expressing GFP-rGBD, max. projection of 5 0.6 micron sections, 6 sec/frame at 30 fps (time in min:sec). Corresponds to Figure 3d. This sequence covers first meiosis in a slightly compressed oocyte. Likely due to the compression, polar body emission fails in this case; nevertheless, the sequence of events is otherwise normal: Rho activity begins at the end of M-phase at the vegetal pole, thus sweeping in from the left edge in this view. The macro-wave of Rho activation can be seen to consist of many short-lived low-amplitude wavelets that scatter like chop in a sea breeze. While the cytokinetic zone is more persistent, flickers reveal that it too consists of a flock of similar wavelets.

Supplementary Video 9 One of four cells in a normal starfish embryo expressing both GFP-rGBD (malachite) and mCherry-Utr (copper), max. projection of 14 0.6 micron sections, 17 sec/frame at 15 fps (time in min:sec). Corresponds to Figure 4a. Cytokinetic Rho activity begins with a transient, global but non-uniform pulse, rapidly focusing at the equator. Wavelets similar in size to those observed in oocytes populate the early furrow. F-actin enrichment does not overlap perfectly with Rho activity; rather, F-actin enrichment develops in the wake of Rho activity waves.

Supplementary Video 10 Starfish oocyte expressing both GFP-rGBD (malachite) and mCherry-Utr (copper), plus wild-type *S. purpuratus* Ect2. Projection of 14 0.8 micron sections, 17 sec/frame at 20 fps (time in min:sec). Corresponds to Figure 4c. In this nearly-animal-pole view, the site of meiosis is just out of view beyond the bottom of the frame. F-actin waves consistently follow, rather than overlap with, Rho waves, and Rho waves move into F-actin-poor zones.

Supplementary Video 11 Activated frog egg expressing GFP-rGBD (malachite) and mCherry-Utr (copper), plus wild-type *Xenopus* Ect2, average projection of 4 1 micron sections, 10 sec/frame at 20 fps (time in min:sec). Corresponds to Fig. 4d. Rho activity waves and F-actin assembly waves have similar forms but at successive times; consequently, there is little overlap between wave peaks. Thus, throughout this sequence very little yellow (indicating colocalization) intercedes between malachite and copper.

Supplementary Video 12 Starfish zygote expressing GFP-rGBD (malachite) and mCherry-Utr (copper), plus wild type *S. purpuratus* Ect2, max. projection of 5 0.5 micron sections, 6 sec/frame at 20 fps (time in min:sec). Corresponds to Fig. 4e. This sequence begins in M-phase, with a relatively uniform F-actin carpet dominated by microvilli, and low-amplitude Rho activity waves. At anaphase Rho waves rapidly build to a near-uniform peak as microvilli give way to a finer-textured F-actin cortical layer, which in turn quickly breaks into waves as the cytokinetic zone develops. As furrow ingression proceeds, Rho/F-actin waves continue in tropical and polar regions. Little yellow is evident between malachite and copper fronts, but distinct dark areas separate advancing malachite front from trailing edges of copper waves.

Supplementary Video 13 Reconstruction of excitable phase on the cortex of starfish oocyte overexpressing Ect2 permits to reveal spiral wave cores. Phase (right panel) is color-coded as in Figure 5. Arrowhead points to a spiral wave core that persists for nearly 59 min. Corresponding Rho activity signal (GFP-rGBD) is shown for comparison (right panel). Note that no spiral wave is readily distinguishable in the Rho activity pattern by naked eye. Corresponds to Figure 5d-f. Frame rate is 41.3 sec.

Supplementary Video 14 Ect2-expressing starfish oocytes (malachite=GFP-rGBD, copper=mCherry-Utr) exposed to a pipette filled with agarose impregnated with 10 μM Latrunculin B in seawater. Max. projection of 15 1.5 micron sections, 20 sec/frame at 15 fps (time in min:sec). Corresponds to Figure 5g. In the oocyte nearest the drug source, the cortical F-actin rind shatters and melts on the side facing the pipette, accompanied by a surge of Rho activation. On the other side of the oocyte, waves transiently switch to a high-amplitude, long-period regime before the cortical F-actin layer shreds and ultimately collapses there too. In contrast, the oocyte further from the drug source never undergoes complete F-actin disassembly, and, following an initial burst, sustains the high-amplitude long-period wave regime for nearly 10 minutes. Note that because oocytes contain a fixed amount of the Utrophin-based probe for F-actin, even complete disassembly does not change the average fluorescence in the cell.

Supplementary Video 15 Ect2-expressing starfish oocyte (malachite=GFP-rGBD, copper=mCherry-Utr) exposed to a pipette filled with agarose impregnated with 1 μm Latrunculin B in seawater. Max. projection of 19 1 micron sections, 18 sec/frame at 15 fps (time in min:sec). Corresponds to Figure 5h. This oocyte was post-meiotic, and exhibited Ect2-enhanced waves typical for this stage (similar to Fig. 4c), when the pipette was brought close to the right edge. At the applied dose, F-actin never completely disassembled, and indeed new assembly continued throughout the sequence. However, the period and amplitude of Rho/F-actin waves increased dramatically, first near the pipette and then around the entire cell, except in the patch of cortex attached to the coverslip, which apparently experiences lower drug concentration such that the original wavelength remains. The high-amplitude, long-period regime continued for ~30 min. before onset of zygotic M-phase put a stop to excitability.

Supplementary Video 16 Starfish oocytes expressing GFP-rGBD, wild-type *S. purpuratus* Ect2, and Δ90-Cyclin B, treated with Roscovitine. Max. projection of 11 2 micron sections, 19 sec/frame at 30 fps (time in min:sec after Roscovitine treatment). Corresponds to Figure 6e. A group of ~12 oocytes were held tightly packed and slightly compressed between a slide and coverslip; 40 μM Roscovitine was added by perfusing the chamber; the perfusing stream ran SE-NW, and oocytes on the left and lower right were directly exposed to the stream, while the other were partially occluded (note that Z-series did not reach maximum diameter: oocytes on the left side were tightly packed). Roscovitine elicits excitability in the solvent-exposed cells within 5 minutes, culminating in C-phase-like burst of global Rho activation, followed by sustained waves over 2+ hours. Buried oocytes respond later but similarly, with a longer build-up from wave initiation to the global burst of Rho activity.

Supplementary Video 17 Fertilized starfish oocyte expressing GFP-rGBD and wild-type *S. purpuratus* Ect2, cut before 1st meiosis into nucleated and anucleate halves. Max. projection of 14 1 micron sections, 20 sec/frame at 20 fps (time in min:sec). Corresponds to Figure 7a. Upper half contains sperm entry point and meiotic spindle; lower half is anucleate and lacks centrosomes. Both halves become synchronously excitable for 1st meiosis, then 2nd meiosis. This oocyte apparently received a modest dose of Ect2, such that excitability persists only for a short time around meiotic divisions, which both complete successfully in the nucleated half.

Supplementary Video 18 Fertilized starfish oocyte expressing GFP-rGBD (no extra Ect2) and treated with 5 μM nocodazole prior to 1st meiosis. Max. projection of 14 0.6 micron sections, 16 sec/frame at 20 fps (time in min:sec). Corresponds to Figure 7e. Sperm entry point is visible to the lower left, meiotic spindle to the upper right. Vegetal-to-animal "macro-waves" of Rho activation proceed as normal, except that instead of culminating in a cytokinetic zone they reach the animal pole and dissipate. There is no zone of Rho suppression around the site of meiosis, as there normally would be; indeed, the very animal pole exhibits peak Rho activity, and even persistent activity between divisions.

Supplementary Video 19 Simulation of the excitable dynamics on the cortex of starfish oocyte undergoing meiosis. Rho activity and F-actin density are color-coded as in Figure 8. Note a striking change in the wave pattern during the increase in global Ect2 activity that represents the polar body extrusion phase (see Methods for details). Compare with Supplementary Figure 6d. Corresponds to Figure 8a-c.

Supplementary Video 20 Simulation of the furrow formation in mitotic starfish blastomere. Rho activity and F-actin density are color-coded as in Figure 8. During the simulation spatial distribution of cortical Ect2 is focused towards the equator to imitate the microtubule-dependent translocation (see Methods for details). Compare with Figures 3e, 4a. Corresponds to Figure 8d,e.

Supplementary Video 21 GFP-rGBD- and Ect2-expressing starfish embryo treated with 40 μM nocodazole during cytokinesis. Max. projection of 8 1 micron sections, 20 sec/frame at 20 fps (time in min:sec after nocodazole treatment). Corresponds to Figure 8h. A binucleate cell that had failed first cleavage was chosen, because at the time of treatment it displays a) prominent cytokinetic Rho zones, b) a spindle-distant zone to the left populated by distinct waves, and c) spindle-proximal zones that lack waves. Nocodazole treatment abolishes the cytokinetic Rho zones and low-level waves repopulate the entire surface as furrows regress; waves disappear after ~30 min. as next M-phase commences.

Supplementary Video 22 GFP-rGBD in a normal cleaving blastomere from a 16-cell starfish embryo. Max. projection of 42 0.5 micron sections, 12 sec/frame at 15 fps. Corresponds to Supplementary Figure 3b. A narrow strip around the equator was imaged so as to capture ~one-third of the entire furrow circumference as it ingresses. Animation leaves kymograph (as in Sup. Fig. 3b) in its wake. Blotches of Rho activity at each time point actually represent waves within the furrow.

Supplementary Video 23 GFP-rGBD in a normal 64-cell starfish embryo, four cells. Max. projection of 16 0.6 micron sections, 9 sec/frame at 15 fps. Corresponds to Supplementary Figure 3c. At this stage, furrow zones are coherent but still clearly exhibit waves during zone formation and initial ingression.

Supplementary Video 24 GFP-rGBD in a normal starfish embryo, 128+ cells. Max. projection of 12 0.8 micron sections, 14 sec/frame at 15 fps. Corresponds to Supplementary Figure 3d. As cell size decreases throughout embryogenesis, waves are less apparent in cleavage furrows. Rho activity zones are initially inhomogeneous, but rapidly cohere as ingression proceeds.